

Oscillatory Dynamics for a Coupled Membrane-Bulk Diffusion Model with Fitzhugh-Nagumo Membrane Kinetics

J. GOU, M. J. WARD

Jia Gou, Michael Ward; Department of Mathematics, Univ. of British Columbia, Vancouver, B.C., V6T 1Z2, Canada.

(Received 5 January 2016)

Oscillatory dynamics associated with the coupled membrane-bulk PDE-ODE model of Gomez et al. [Phys. Rev. Lett., **98**(16), (2007), 168303] in one spatial dimension is analyzed using a combination of asymptotic analysis, linear stability theory, and numerical bifurcation software. The mathematical model consists of two dynamically active membranes with Fitzhugh-Nagumo kinetics, separated spatially by a distance L , that are coupled together through a diffusion field that occupies the bulk region $0 < x < L$. The flux of the diffusion field on the membranes at $x = 0$ and $x = L$ provides feedback to the local dynamics on the membranes. In the absence of membrane-bulk coupling the membrane kinetics have a stable fixed point. The effect of bulk diffusion is to trigger either synchronous and asynchronous oscillations in the two membranes. In the singular limit of slow-fast membrane dynamics, and with only one diffusing species in the bulk, phase diagrams in parameter space showing where either synchronous or asynchronous oscillations occur, together with the corresponding Hopf frequencies at onset, are provided analytically. When the membrane kinetics is not of slow-fast type, a numerical study of the stability problem together with the numerical bifurcation software XPPAUT [7] is used to construct global bifurcation diagrams of steady-states and the bifurcating periodic solution branches for the case of either one or two diffusing species in the bulk. Overall, our results show the existence of a wide parameter range where stable synchronous oscillatory dynamics in the two membranes can occur. Predictions from the analytical and bifurcation theory are confirmed with full numerical simulations of the PDE-ODE system.

Key words: Bulk diffusion, active membranes, Hopf bifurcation, winding number, synchronous oscillations.

1 Introduction

We analyze a coupled PDE-ODE model that leads to the collective synchronization of oscillatory dynamics for spatially segregated, but dynamically active, regions that are coupled spatially through a linear bulk diffusion field. The coupling of dynamically active membranes or spatially localized compartments, modeled by ODE dynamics, through a linear bulk diffusion field, arises in many different applications. A well-known example involves the signalling of the amoebae *Dictyostelium discoideum* through the release of cAMP into the medium where it diffuses and acts on other amoeba in the colony (cf. [8]). Some models of related quorum sensing behavior are given in [6], [20], and [21]. In the modeling of catalytic reactions occurring on solid surfaces, it was shown in [16] that oscillations in the surface kinetics are triggered by the effect of spatial bulk diffusion in the gas phase near the catalytic surface. Related models of the effect of the coupling of diffusion to localized chemical reactions are given in [24], [26], [28], and [22]. Other applications include the analysis of Turing patterns arising from coupled bulk and surface diffusion (cf. [17]). In the study of cellular signal transduction, [15] emphasizes the need for developing detailed models of cell signaling that are not strictly ODE based, but that, instead, involve spatial diffusion processes coupled with bio-chemical reactions occurring within localized signaling compartments.

A more traditional modeling framework that is well-known to lead to the synchronization of dynamically active units are the ODE-based models, originating in [1] and [29], that couple nonlinear oscillators, each having a stable rest point in isolation from its neighbours, through various coupling mechanisms. In the asymptotic limit of weak coupling, the study of oscillator synchronization on an ODE network is typically done using a phase-reduction approach (see [23] and the

references therein). A recent survey of weakly coupled oscillator theory for deterministic and stochastic ODE systems, with applications to neuroscience, is given in [2]. In contrast, there are rather few analytical studies of oscillator synchronization for PDE-ODE models. In the context of neuroscience, PDE-ODE models for dendritic oscillations arising from coupling through a passive cable have been developed in [25] and [27]. For these models, oscillator synchronization was analyzed in the limit of weak dendrite-cable coupling by extending the phase-reduction method (cf. [23]) to a PDE context.

In this broad context, the goal of this paper is to give a detailed analysis of the triggering of synchronous oscillations for the 1-D coupled membrane-bulk model of [9]. This PDE-ODE model of [9] consists of two active membranes with activator-inhibitor dynamics at $x = 0, L$ that are coupled through passive diffusion in the bulk region $0 < x < L$. In the bulk, there are two diffusing species with concentrations $U(x, t)$ and $V(x, t)$ satisfying

$$(1.1 a) \quad U_t = D_u U_{xx} - \sigma_u U, \quad V_t = D_v V_{xx} - \sigma_v V, \quad 0 < x < L, \quad t > 0.$$

Here D_u and D_v are the two diffusion coefficients, while σ_u and σ_v are the constant bulk decay rates. The kinetics on the two active membranes at $x = 0$ and $x = L$ are assumed to be identical, and given by

$$(1.1 b) \quad \begin{aligned} u'_1 &= f(u_1, v_1) + k_u U_x(0, t), & v'_1 &= \epsilon g(u_1, v_1) + k_v V_x(0, t), \\ u'_2 &= f(u_2, v_2) - k_u U_x(L, t), & v'_2 &= \epsilon g(u_2, v_2) - k_v V_x(L, t), \end{aligned}$$

where u_i and v_i , $i = 1, 2$ denote the two concentrations on the membrane, so that $u_1(t) = U(0, t)$, $u_2(t) = U(L, t)$, $v_1(t) = V(0, t)$ and $v_2 = V(L, t)$. The parameter ϵ that accompanies $g(u_i, v_i)$ determines the relative difference in the time-scale for the boundary kinetics, so that the time evolution of u is much faster than v if $0 < \epsilon \ll 1$. The terms $k_u U_x(0, t)$ and $k_v V_x(0, t)$ account for the exchange of species between the membrane and the bulk, where the constants k_u and k_v are called the leakage parameters. The kinetics $f(u, v)$ and $g(u, v)$, modeling a local activator-inhibitor dynamics, are taken to be the Fitzhugh-Nagumo type kinetics considered in [9], given for $q > 0$ and $z > 0$ by

$$(1.1 c) \quad f(u, v) = u - q(u - 2)^3 + 4 - v, \quad g(u, v) = uz - v.$$

In our analysis we will either consider the strong coupling limit where $\epsilon = \mathcal{O}(1)$ and $k_u = k_v = \mathcal{O}(1)$, or the singularly perturbed limit $\epsilon \ll 1$ with $k_v = \mathcal{O}(\epsilon)$ and $k_u = \mathcal{O}(1)$ of slow-fast membrane dynamics. As such, since we do not assume a weak coupling between the membrane and the bulk, the phase-reduction methodology of [25] and [27] does not appear to be an appropriate tool for the analysis of (1.1).

To illustrate the phenomena to be analyzed, in Fig. 1 we show a contour plot of $V(x, t)$ together with the time-history of the two membrane components, as computed numerically from (1.1) on a domain of length $L = 4$, for the bulk parameters $D_v = 0.5$, $D_u = 1.5$, $\sigma_v = 0.008$, and $\sigma_u = 0.01$, the Fitzhugh-Nagumo parameters $z = 3.5$ and $q = 5$, the leakage parameters $k_u = k_v = 0.7$, and with $\epsilon = 0.15$. For $z = 3.5$ and $q = 5$, the membrane dynamics have a unique stable steady-state when uncoupled from the bulk. For the initial condition as given in the figure caption, Fig. 1 shows that the coupling of the two membranes by bulk diffusion triggers oscillations that otherwise would not be present, and that the membrane oscillations become synchronized as time increases. One goal of this paper is to develop analytical and numerical tools to identify parameter regimes for the existence of such synchronized membrane-bulk oscillations for (1.1).

In contrast to the regime where $\epsilon = \mathcal{O}(1)$, for the singular slow-fast limit where $\epsilon \rightarrow 0$, the qualitative mechanism for the triggering of time-periodic solutions for the coupled system (1.1), as discussed in [9], is based on a simple nullcline analysis, and is described in the caption of Fig. 2. We assume that q and z are chosen such that the membrane kinetics in the absence of any coupling to the bulk has a single stable equilibrium point. For $q = 5$ and $z = 3.5$, this stable fixed point (u_e, v_e) occurs at the intersection of the two nullclines $v = \mathcal{V}(u) = u - q(u - 2)^3 + 4$ and $v = zu$ where $f(u, \mathcal{V}(u)) = 0$

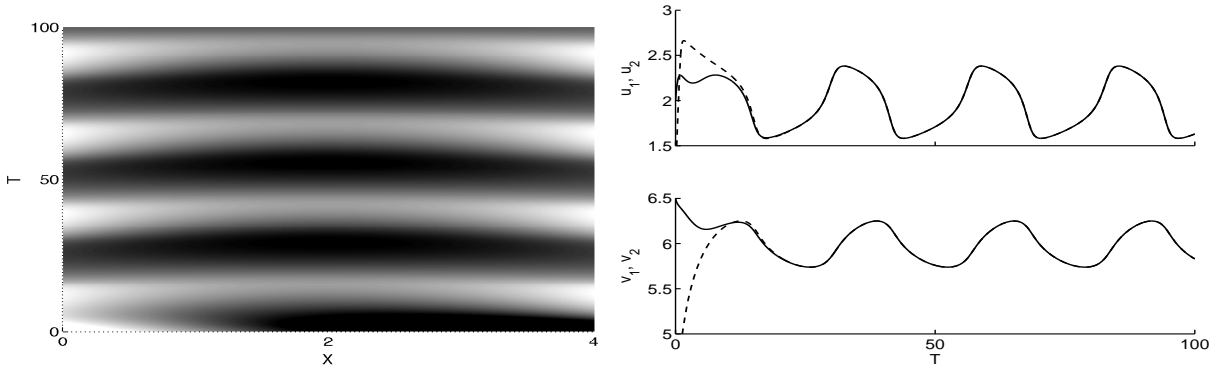


Figure 1. Left: contour plot of numerical solution for $V(x, t)$, computed from the PDE-ODE system (1.1), showing stable synchronous oscillations for the bulk parameter values $D_v = 0.5$, $D_u = 1.5$, $\sigma_v = 0.008$, and $\sigma_u = 0.01$, the Fitzhugh-Nagumo parameters $z = 3.5$ and $q = 5$, the leakage parameters $k_u = k_v = 0.7$, and with $\epsilon = 0.15$ and $L = 4$. The initial condition for (1.1) was $V(x, 0) = 6.5 - x/2$, $U(x, 0) = 2 \sin(x) + 2$, $u_1 = 2$, $u_2 = 0.48$, $v_1 = 6.5$, $v_2 = 4.5$, at $t = 0$. Right panel: plot of the two membrane components in the two separate compartments versus t .

and $g(u, zu) = 0$. In the limit $\epsilon \rightarrow 0$, it is readily shown from the Jacobian of the membrane kinetics that the equilibrium (u_e, v_e) is linearly stable only when $\mathcal{V}'(u_e) < 0$, and undergoes a Hopf bifurcation when $\mathcal{V}'(u_e)$ crosses through zero. When the leakages in (1.1 b) satisfy $k_u = \mathcal{O}(\epsilon)$ and $k_v = \mathcal{O}(\epsilon)$, we have, to leading order in ϵ , that the steady-state of (1.1 b) remains on the nullcline $f(u, v) = 0$. However, the effect of the coupling to the bulk for V is to shift the nullcline for the v -component in (1.1 b) to $v = \beta u$, for some β that is a monotonically decreasing function of k_v . This shows that there is an intermediate range of β where the equilibrium point is unstable, as given by the dotted line in Fig. 2. Although this mechanism of [9] does explain qualitatively why triggered oscillations can be induced by membrane-bulk coupling in the limit $\epsilon \rightarrow 0$, it does not provide a detailed quantitative characterization of these oscillations.

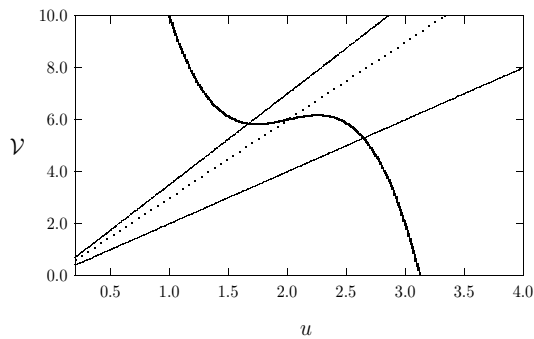


Figure 2. Plot of the nullcline $\mathcal{V}(u) = u - q(u - 2)^3 + 4$ with $q = 5$ for which $f(u, \mathcal{V}(u)) = 0$. The straight lines are $v = \beta u$ with $\beta = 3.5$, $\beta = 3$, and $\beta = 2$. The straight line $v = 3.5u$ is the nullcline of $g(u, v) = 0$ when $z = 3.5$ for the uncoupled membrane-bulk problem. As the leakage $k_v = \mathcal{O}(\epsilon)$ increases, the effective parameter β decreases. The dotted line with $\beta = 3$ intersects $\mathcal{V}(u)$ in the unstable region where $\mathcal{V}'(u) > 0$. For $\beta = 2.0$, the intersection again occurs in the stable region for the membrane kinetics. For a leakage where $k_u = \mathcal{O}(\epsilon)$ in (1.1 b) the nullcline for $f(u, v) = 0$ is, to leading order in ϵ , unchanged by the coupling of the membrane to the bulk.

As an extension of this qualitative and numerical analysis of [9], we use asymptotic analysis together with bifurcation and stability theory to give a detailed theoretical analysis of the onset of oscillatory dynamics for (1.1). In the singular limit $\epsilon \rightarrow 0$ of slow-fast membrane dynamics, and assuming only one diffusing species in the bulk, our stability analysis of

the unique symmetric steady-state solution will provide a detailed phase diagram in parameter space where various types of oscillatory dynamics can occur. In the limit $\epsilon \rightarrow 0$, our asymptotic analysis of the spectral problem, and in particular the winding number, will yield asymptotic approximations for the Hopf bifurcation thresholds in parameter space for both the synchronous and asynchronous periodic solution branches, as well as the Hopf bifurcation frequencies near onset. In addition, zero-eigenvalue crossings corresponding to the emergence of asymmetric steady-state solutions will be studied.

In the non-singular case, where $\epsilon = \mathcal{O}(1)$, a numerical study of the winding number is used to determine a phase diagram in parameter space where the steady-state solution is linearly unstable and to determine the boundaries in this parameter space where Hopf bifurcations can occur. To examine, in a more global sense, the behavior of the large amplitude solutions that emerge from these bifurcation points of the linearization of the steady-state we use the numerical bifurcation software XPPAUT [7]. In this way, we obtain a global bifurcation diagram of steady-state and large amplitude periodic solution branches for the case of either one or two diffusing species in the bulk. Overall, this hybrid analytical-numerical approach shows that stable synchronous large-amplitude oscillations between the two membranes is a robust feature of the dynamics that occurs in a wide parameter regime. The numerical results shown in Fig. 1 correspond to a particular parameter set where synchronized oscillations between the two membranes is predicted from our theory in §4. Moreover, a glimpse at some more exotic dynamics such as a torus bifurcation, arising from secondary bifurcations, is also given.

Although our analysis is based on a specific reaction kinetics on the two membranes, the mechanism through which oscillatory dynamics occur is similar for other membrane kinetics. In [11] a bifurcation analysis of coupled membrane-bulk oscillatory dynamics with Sel'kov membrane kinetics was given. However, for the model of [11], where the membrane dynamics was not of slow-fast type, comparatively little analysis of the oscillatory dynamics was possible. In the related article [12], a detailed linear stability theory was given for a general class of coupled membrane-bulk models with only one active component on the membrane. For this class, a weakly nonlinear analysis, leading to an amplitude equation, was developed to characterize whether Hopf bifurcations from the steady-state are subcritical or supercritical.

The outline of this paper is as follows. In § 2 we construct a symmetric steady-state solution, and we formulate the linear stability problem for this solution. In § 3 we consider a one-bulk species model where only the inhibitor V can diffuse in the bulk. For this case, in § 3.1 an asymptotic analysis for $\epsilon \rightarrow 0$ of the stability problem is provided to analyze Hopf bifurcations of the symmetric steady-state and the emergence of asymmetric steady-states. The $\epsilon = \mathcal{O}(1)$ problem for one diffusing bulk species is studied numerically in §3.2. In § 4 we extend our analysis to the full model (1.1) consisting of two diffusing bulk species. A brief qualitative summary of our results and suggestions for further work is given in § 5.

2 The Steady-State Solution and the Formulation of the Linear Stability Problem

In this section we determine a symmetric steady-state solution for (1.1) and analyze the linear stability properties of this solution. Since the two membranes are identical, it is natural to seek a steady-state solution that is symmetric about the midline $x = L/2$, so that for the steady-state problem of (1.1) we consider $0 < x < L/2$ and impose zero flux conditions at $x = L/2$. In the steady-state analysis, for convenience we drop the subscripts for u and v at the left membrane. As such, the symmetric steady-state solution U_e and V_e for (1.1) satisfies

$$(2.1) \quad D_u U_{exx} - \sigma_u U_e = 0, \quad D_v V_{exx} - \sigma_v V_e = 0, \quad 0 < x < L/2,$$

with boundary conditions $U_e(0) = u_e$, $V_e(0) = v_e$, $U_{ex}(L/2) = 0$, and $V_{ex}(L/2) = 0$. The solution to this problem is

$$(2.2) \quad U_e(x) = u_e \frac{\cosh[\omega_u(\frac{L}{2} - x)]}{\cosh(\omega_u L/2)}, \quad V_e(x) = v_e \frac{\cosh[\omega_v(\frac{L}{2} - x)]}{\cosh(\omega_v L/2)}, \quad \omega_u \equiv \sqrt{\frac{\sigma_u}{D_u}}, \quad \omega_v \equiv \sqrt{\frac{\sigma_v}{D_v}}.$$

Then, by using (1.1 b) with kinetics (1.1 c), we readily derive that $u = u_e$ is a root of the cubic $\mathcal{H}(u) = 0$, given by

$$(2.3 a) \quad \mathcal{H}(u) \equiv qu^3 - 6qu^2 + (12q - 1 + a_u + \beta) u - (8q + 4),$$

where we have defined a_u and β , by

$$(2.3 b) \quad a_u \equiv k_u \omega_u \tanh(\omega_u L/2), \quad \beta \equiv \epsilon z / (\epsilon + a_v), \quad \text{where} \quad a_v \equiv k_v \omega_v \tanh(\omega_v L/2).$$

In terms of any solution $u = u_e$ to the cubic, v_e is given by $v_e = \beta u_e$.

We now claim that (1.1) has a unique positive symmetric steady-state solution. To show this, we must verify that there is a unique root $u_e > 0$ to $\mathcal{H}(u) = 0$ when $u > 0$. In our proof below we will consider two cases: Case I: $a_u + \beta > 1$. Case II: $0 < a_u + \beta \leq 1$. We first consider Case I. We calculate that $\mathcal{H}(0) = -(8q + 4) < 0$ and $\mathcal{H}(u) \rightarrow +\infty$ as $u \rightarrow +\infty$. Moreover, we derive that $\mathcal{H}'(u) = 3q(u - 2)^2 + (a_u + \beta - 1)$, so that $\mathcal{H}'(u) > 0$ for $u > 0$ in Case I. Since $\mathcal{H}(0) < 0$, $\mathcal{H}(u) \rightarrow +\infty$ as $u \rightarrow \infty$, and $\mathcal{H}(u)$ is monotone increasing on $u > 0$, there is a unique root to $\mathcal{H}(u) = 0$ in $u > 0$ in Case I.

Next, we consider Case II. We conclude that $\mathcal{H}'(u) = 0$ at exactly two points $u = u_{\pm}$, given by

$$(2.4) \quad u_{\pm} \equiv 2 \pm \frac{1}{\sqrt{3q}} \sqrt{1 - a_u - \beta}.$$

Here $u_- < 2 < u_+$, with u_- and u_+ a local maximum and local minimum of $\mathcal{H}(u)$, respectively. Therefore, since $2 < u_+$, $\mathcal{H}(2) = -6 + 2(a_u + \beta) < 0$, $\mathcal{H}(u) \rightarrow +\infty$ as $u \rightarrow \infty$, and u_+ is a local minimum point of $\mathcal{H}(u)$, we conclude that there is a unique root to $\mathcal{H}(u) = 0$ in $u > 2$. To conclude the proof for Case II, we need only show that $\mathcal{H}(u_-) < 0$ whenever u_- is on the range $0 < u_- < 2$. To show this we use $3q(u_- - 2)^2 = 1 - (a_u + \beta)$ to calculate

$$\begin{aligned} \mathcal{H}(u_-) &= q(u_- - 2)^3 - u_- - 4 + (a_u + \beta) u_- = \frac{[1 - (\beta + a_u)]}{3} (u_- - 2) - u_- - 4 + (a_u + \beta) u_-, \\ &= \frac{1}{3} (-2u_- [1 - (a_u + \beta)] - 14 + 2(a_u + \beta)). \end{aligned}$$

Since the last expression shows that $\mathcal{H}(u_-) < 0$ for $0 < u_- < 2$ when $0 < a_u + \beta \leq 1$, we conclude that there are no additional roots to $\mathcal{H}(u) = 0$ located on $0 < u < 2$ whenever $0 < a_u + \beta \leq 1$. Combining the results of Case I and Case II, we conclude that, for any $a_u + \beta > 0$, there is a unique positive symmetric steady-state solution to (1.1).

We will assume that z and q are such that the steady-state of the membrane kinetics, when uncoupled to the bulk, is a linearly stable fixed point. As a result, any instability that arises in our analysis is due specifically to the coupling of the two membranes by the bulk. For the uncoupled problem, where $a_u = 0$ and $a_v = 0$ in (2.3), we obtain that u_e is a root of (2.3 a) in which we set $a_u = 0$ and $\beta = z$ in (2.3 a). In terms of u_e , the Jacobian of the membrane kinetics is

$$(2.5) \quad J_e^0 \equiv \begin{pmatrix} f_u^e & f_v^e \\ \epsilon g_u^e & \epsilon g_v^e \end{pmatrix} = \begin{pmatrix} 1 - 3q(u_e - 2)^2 & -1 \\ \epsilon z & -\epsilon \end{pmatrix},$$

when uncoupled from the bulk. We calculate the determinant and trace of this matrix as

$$(2.6) \quad \det J_e^0 = \epsilon [z - 1 + 3q(u_e - 2)^2], \quad \text{tr} J_e^0 = 1 - \epsilon - 3q(u_e - 2)^2.$$

To ensure that the uncoupled membrane kinetics has a stable fixed point, we will assume that $z > 1$, so that $\det J_e^0 > 0$ for any parameter set. Therefore, the stability of the fixed point is determined by the sign of $\text{tr} J_e^0$. To determine the region of the (q, z) plane, with $z > 1$, for which $\text{tr} J_e^0 < 0$, we simply locate the stability boundary where $\text{tr} J_e^0 = 0$. We solve (2.6) for q and then (2.3 a), with $a_u = 0$ and $\beta = z$, for z , to readily obtain a parametric description of this stability boundary in the form $q = Q(u)$ and $z = Z(u)$, for $u \geq 0$, where

$$(2.7) \quad q = Q(u) \equiv \frac{(1 - \epsilon)}{3(u - 2)^2}, \quad z = Z(u) \equiv 1 + \frac{4}{u} - \frac{(1 - \epsilon)}{3u} (u - 2).$$

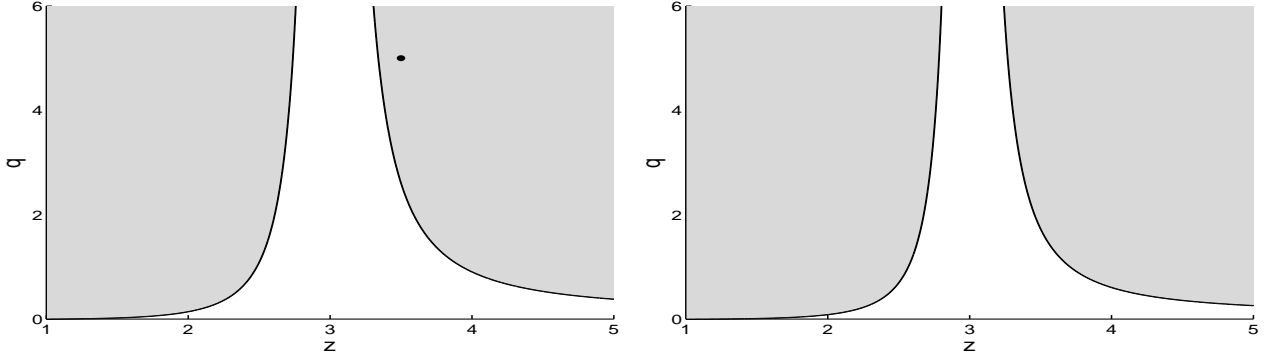


Figure 3. The stability boundary when $\epsilon = 0.015$ (left panel) and when $\epsilon = 0.3$ (right panel) for the membrane dynamics when uncoupled to the bulk diffusion. The heavy solid curve is the stability boundary (2.7) where $\text{tr}J_e^0 = 0$. Above this curve in the shaded region, $\text{tr}J_e^0 < 0$ so that the uncoupled membrane kinetics has a stable fixed point in this region. For $\epsilon = 0.015$, the parameter values $z = 3.5$ and $q = 5$, used in [9], correspond to the marked point.

For $\epsilon = 0.015$ and $\epsilon = 0.3$ in the left and right panels of Fig. 3, respectively, we plot the stability boundary (2.7) for the uncoupled problem in the (q, z) plane for $z > 1$. In the shaded regions of this figure we have $\text{tr}J_e^0 < 0$. In our analysis below, we will assume that the pair (q, z) belongs to this region, which ensures that the fixed point associated with the uncoupled membrane kinetics is linearly stable. As a remark, for the parameter values $z = 3.5$, $q = 5.0$, and $\epsilon = 0.015$, as used in [9], we calculate from (2.3 a) and (2.6) that $u_e \approx 1.67$ and $\text{tr}J_e^0 \approx -0.649 < 0$, so that the fixed point for the uncoupled dynamics is stable. This point is marked in the left panel of Fig. 3.

2.1 Formulation of the Linear Stability Problem

Next, we derive the linear stability problem associated with the symmetric steady-state solution. We introduce

$$U(x, t) = U_e(x) + \varphi(x)e^{\lambda t}, \quad u(t) = u_e + \xi e^{\lambda t}, \quad V(x, t) = V_e(x) + \psi(x)e^{\lambda t}, \quad v(t) = v_e + \eta e^{\lambda t},$$

into (1.1). Upon linearizing the resulting system we obtain that

$$(2.8 a) \quad D_u \varphi_{xx} - (\sigma_u + \lambda)\varphi = 0, \quad D_v \psi_{xx} - (\sigma_v + \lambda)\psi = 0, \quad 0 < x < L/2,$$

with $\varphi(0) = \xi$ and $\psi(0) = \eta$, together with the linearized membrane kinetics on $x = 0$ given by

$$(2.8 b) \quad \xi \lambda = \xi f_u^e + \eta f_v^e + k_u \varphi'(0), \quad \eta \lambda = \epsilon \xi g_u^e + \eta g_v^e + k_v \psi'(0).$$

Since the two membranes, located at $x = 0$ and at $x = L$, are identical, then due to reflection symmetry there are two types of eigenfunctions for (2.8). These are the synchronous (in-phase) or asynchronous (anti-phase) modes, which satisfy

$$(2.9) \quad \varphi'(L/2) = 0, \quad \psi'(L/2) = 0, \quad (\text{sync}); \quad \varphi(L/2) = 0, \quad \psi(L/2) = 0, \quad (\text{async}).$$

Upon solving (2.8) for the in-phase, or synchronous ('+') mode, we get

$$(2.10) \quad \varphi_+(x) = \xi \frac{\cosh[\Omega_u(\frac{L}{2} - x)]}{\cosh(\Omega_u L/2)}, \quad \psi_+(x) = \eta \frac{\cosh[\Omega_v(\frac{L}{2} - x)]}{\cosh(\Omega_v L/2)},$$

where we have defined $\Omega_u = \Omega_u(\lambda)$ and $\Omega_v = \Omega_v(\lambda)$ by

$$(2.11) \quad \Omega_u \equiv \sqrt{\frac{\sigma_u + \lambda}{D_u}}, \quad \Omega_v \equiv \sqrt{\frac{\sigma_v + \lambda}{D_v}}.$$

In (2.11) we have chosen the principal value of the square root, which ensures that φ_+ and ψ_+ are analytic in $\text{Re}(\lambda) > 0$ and decay at $x = L/2$ when $L \gg 1$. By substituting (2.10) into the boundary condition (2.8 b) at $x = 0$, we get that ξ and η satisfy the homogeneous linear system

$$(2.12) \quad (f_u^e - \lambda - k_u p_+ \Omega_u) \xi + f_v^e \eta = 0, \quad \epsilon g_u^e \xi + (\epsilon g_v^e - \lambda - k_v q_+ \Omega_v) \eta = 0,$$

where we have defined $p_+ = p_+(\lambda)$ and $q_+ = q_+(\lambda)$ by

$$(2.13) \quad p_+ \equiv \tanh(\Omega_u L/2), \quad q_+ \equiv \tanh(\Omega_v L/2).$$

By setting the determinant of the coefficient matrix of this linear system to zero, this linear system has a nontrivial solution if and only if λ is a root of the transcendental equation

$$(2.14) \quad (f_u^e - \lambda - k_u p_+ \Omega_u) (\epsilon g_v^e - \lambda - k_v q_+ \Omega_v) - \epsilon f_v^e g_u^e = 0.$$

Similarly, for the anti-phase, or asynchronous ('-'), mode we obtain from (2.8 a) and (2.9) that

$$\varphi_-(x) = \xi \frac{\sinh[\Omega_u(\frac{L}{2} - x)]}{\sinh(\Omega_u L/2)}, \quad \psi_-(x) = \eta \frac{\sinh[\Omega_v(\frac{L}{2} - x)]}{\sinh(\Omega_v L/2)},$$

where λ satisfies

$$(2.15) \quad (f_u^e - \lambda - k_u p_- \Omega_u) (\epsilon g_v^e - \lambda - k_v q_- \Omega_v) - \epsilon f_v^e g_u^e = 0.$$

Here we have defined $p_- = p_-(\lambda)$ and $q_- = q_-(\lambda)$ by

$$(2.16) \quad p_- \equiv \coth(\Omega_u L/2), \quad q_- \equiv \coth(\Omega_v L/2).$$

The eigenvalue problems (2.14) and (2.15) for the synchronous and asynchronous modes can be written in terms of locating the roots λ of $\mathcal{F}_\pm(\lambda) = 0$, where

$$(2.17) \quad \mathcal{F}_\pm(\lambda) \equiv \frac{1}{k_u k_v p_\pm q_\pm} + \frac{\Omega_u \Omega_v}{\det(J_e - \lambda I)} - \frac{\Omega_u (\epsilon g_v^e - \lambda)}{k_v q_\pm \det(J_e - \lambda I)} - \frac{\Omega_v (f_u^e - \lambda)}{k_u p_\pm \det(J_e - \lambda I)}.$$

Here J_e is the Jacobian matrix of the membrane dynamics (1.1 b), evaluated at the steady-state solution associated with the coupled membrane-bulk model. Therefore, from (2.6), we have

$$(2.18) \quad \det(J_e - \lambda I) = \lambda^2 - (\text{tr} J_e) \lambda + \det J_e, \quad \text{tr} J_e = 1 - \epsilon - 3q(u_e - 2)^2, \quad \det J_e = \epsilon [z - 1 + 3q(u_e - 2)^2],$$

where u_e is the unique root of $\mathcal{H}(u) = 0$, with $\mathcal{H}(u)$ as defined in (2.3 a). In (2.17) we have $\epsilon g_v^e = -\epsilon$ and $f_u^e = \text{tr} J_e + \epsilon$.

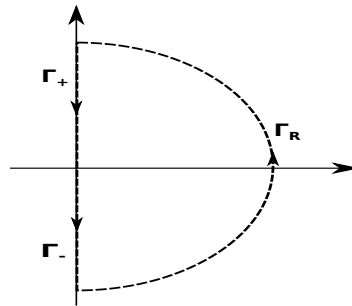


Figure 4. Counterclockwise contour consisting of the imaginary axis $-iR \leq \text{Im}\lambda \leq iR$, denoted by $\Gamma_- \cup \Gamma_+$, and the semicircle Γ_R , given by $|\lambda| = R > 0$, for $|\arg\lambda| \leq \pi/2$.

To analyze the stability of the steady-state solution, we use the argument principle of complex analysis to count the

number N of roots of $\mathcal{F}_\pm(\lambda) = 0$ in the right half-plane $\text{Re}(\lambda) > 0$. We take the counterclockwise contour consisting of the imaginary axis $-iR \leq \text{Im}\lambda \leq iR$, denoted by $\Gamma_- \cup \Gamma_+$, and the semicircle Γ_R , given by $|\lambda| = R > 0$, for $|\arg\lambda| \leq \pi/2$, as shown in Fig. 4. Since $1/p_\pm$, $1/q_\pm$, Ω_u , and Ω_v are analytic functions of λ in the right half-plane $\text{Re}\lambda > 0$, and $\det J_e > 0$ since $z > 1$, it follows that the number P of poles of $\mathcal{F}_\pm(\lambda)$ in the right half-plane depends only on the sign of $\text{tr}J_e$.

Since $p_\pm \rightarrow 1$ and $q_\pm \rightarrow 1$ as $R \rightarrow \infty$ on Γ_R , with $\lambda = Re^{i\omega}$ and $|\omega| \leq \pi/2$, we have that the decay of $\mathcal{F}_\pm(\lambda)$ as $R \rightarrow \infty$ is dominated by the first term in (2.17), so that

$$\mathcal{F}_\pm(\lambda) = \frac{1}{k_u k_v} + \mathcal{O}\left(R^{-1/2}\right), \quad \text{as } R \rightarrow \infty,$$

on Γ_R . Therefore, there is no change in the argument of $\mathcal{F}_\pm(\lambda)$ over Γ_R as $R \rightarrow \infty$. By using the argument principle, together with $\mathcal{F}_\pm(\bar{\lambda}) = \overline{\mathcal{F}_\pm(\lambda)}$, we conclude that

$$(2.19) \quad N = P + \frac{1}{\pi} [\arg \mathcal{F}_\pm]_{\Gamma_+}, \quad \text{where} \quad P = \begin{cases} 2 & \text{if } \text{tr}J_e > 0 \\ 0 & \text{if } \text{tr}J_e < 0 \end{cases}.$$

Here $[\arg \mathcal{F}_\pm]_{\Gamma_+}$ denotes the change in the argument of \mathcal{F}_\pm along the semi-infinite imaginary axis $\Gamma_+ = i\lambda_I$, with $0 \leq \lambda_I < \infty$, traversed downwards. When the membrane dynamics are uncoupled with the bulk we have assumed $\text{tr}J_e < 0$, so that $P = 0$. For the coupled problem, we show below that P depends on the strength of the coupling between the membrane and the bulk. We remark that, although, it is analytically intractable to calculate $[\arg \mathcal{F}_\pm]_{\Gamma_+}$, this quantity is easily evaluated numerically after separating $\mathcal{F}_\pm(i\lambda_I)$ into real and imaginary parts. In terms of this readily-computed quantity, the global criterion (2.19) yields the number of unstable eigenvalues of the linearization (2.8) in $\text{Re}(\lambda) > 0$.

In §3 we determine P and $[\arg \mathcal{F}_\pm]_{\Gamma_+}$ for the synchronous and asynchronous modes in the limiting case where there is only one bulk diffusing species. The general case of two diffusing bulk species is considered in §4.

3 One Diffusive Species in the Bulk

In this section we analyze the special case, considered in [9], where there is only one diffusing species in the bulk. As in [9], we assume that only the inhibitor V can detach from the membrane and diffuse and be degraded in the bulk. As such, in this section we consider the limiting problem where $k_u = 0$ in (1.1) so that $U(x, t)$ has no effect on the membrane kinetics, and can be neglected. The one-bulk species model is formulated as

$$(3.1 a) \quad V_t = D_v V_{xx} - \sigma_v V, \quad 0 < x < L, \quad t > 0,$$

coupled to the membrane dynamics $v_1(t) = V(0, t)$ and $v_2(t) = V(L, t)$, where

$$(3.1 b) \quad u'_1 = f(u_1, v_1), \quad v'_1 = \epsilon g(u_1, v_1) + k_v V_x(0, t); \quad u'_2 = f(u_2, v_2), \quad v'_2 = \epsilon g(u_2, v_2) - k_v V_x(L, t).$$

Here $f(u, v)$ and $g(u, v)$ are given in (1.1 c). For this limiting problem, the symmetric steady-state solution satisfies

$$(3.2 a) \quad D_v V_{exx} - \sigma_v V_e = 0, \quad 0 < x < L/2; \quad V_e(0) = v_e, \quad V_{ex}(L/2) = 0,$$

$$(3.2 b) \quad f(u_e, v_e) = 0, \quad \epsilon g(u_e, v_e) + k_v V_{ex}(0) = 0.$$

Defining $\omega_v \equiv \sqrt{\sigma_v/D_v}$, we obtain that u_e is the unique root of $\mathcal{H}(u) = 0$, where

$$(3.3) \quad \mathcal{H}(u) \equiv qu^3 - 6qu^2 + (12q - 1 + \beta)u - (8q + 4); \quad \beta \equiv z/(1 + \epsilon^{-1}a_v), \quad a_v \equiv k_v \omega_v \tanh(\omega_v L/2).$$

By setting $k_u = 0$ in the stability analysis of §2.1, we obtain that the linear stability properties of this symmetric

steady-state is determined by the roots of $\mathcal{G}_{\pm}(\lambda) = 0$, defined by

$$(3.4) \quad \mathcal{G}_{\pm}(\lambda) = \frac{1}{k_v q_{\pm}} - \frac{\Omega_v(f_u^e - \lambda)}{\det(J_e - \lambda I)},$$

where Ω_v , q_+ , and q_- , are defined in (2.11), (2.13), and (2.16), respectively.

To analyze the roots of (3.4), it is convenient to write (3.3) and (3.4) in terms of dimensionless bifurcation parameters. To this end, we introduce two parameter l_1 and l_0 , and define β in (3.3) in terms of them as

$$(3.5) \quad l_1 = k_v/\epsilon, \quad l_0 = \sqrt{D_v/\sigma_v} = 1/\omega_v, \quad \beta = z \left[1 + \frac{l_1}{l_0} \tanh\left(\frac{L}{2l_0}\right) \right]^{-1}.$$

The ratio L/l_0 is a nondimensional measure of the distance between the compartments to the diffusion length l_0 , while l_1/l_0 is a nondimensional measure of the strength of the membrane-bulk coupling relative to the diffusion length.

Next, we define $b \equiv \text{tr}J_e$, and use (2.18) to write

$$(3.6) \quad f_u^e = b + \epsilon, \quad \det J_e = \epsilon a, \quad a \equiv z - \epsilon - b > 0, \quad \text{where } b = 1 - \epsilon - 3q(u_e - 2)^2.$$

We recall that $a > 0$ since we assume from §2 that $z > 1$. In this way, and upon writing q_{\pm} and Ω_v in terms of l_0 and l_1 , we obtain that (3.4) can be written as $\mathcal{G}_{\pm}(\lambda) = [1/(\epsilon l_0)] \mathcal{G}_{\pm}^0(\lambda)$, where $\mathcal{G}_{\pm}^0(\lambda)$ is defined by

$$(3.7) \quad \mathcal{G}_{\pm}^0(\lambda) \equiv \frac{l_0}{l_1 q_{\pm}(\tau_v \lambda)} - \epsilon \sqrt{1 + \tau_v \lambda} \left(\frac{b + \epsilon - \lambda}{\lambda^2 - b\lambda + \epsilon a} \right),$$

where $q_{\pm}(\tau_v \lambda)$, with $\tau_v \equiv 1/\sigma_v$, is defined by

$$(3.8) \quad q_{\pm}(\tau_v \lambda) = \begin{cases} \tanh\left[\frac{L}{2l_0} \sqrt{1 + \tau_v \lambda}\right], & \text{synchronous (+) mode} \\ \coth\left[\frac{L}{2l_0} \sqrt{1 + \tau_v \lambda}\right], & \text{asynchronous (-) mode} \end{cases}.$$

By using a winding number argument, similar to that in §2.1, the number N of unstable roots of (3.7) in $\text{Re}(\lambda) > 0$ is

$$(3.9) \quad N = P + \frac{1}{\pi} [\arg \mathcal{G}_{\pm}^0]_{\Gamma_+}, \quad \text{where } P = \begin{cases} 2 & \text{if } b = \text{tr}J_e > 0 \\ 0 & \text{if } b = \text{tr}J_e < 0 \end{cases}.$$

In terms of our dimensionless parameters, we remark that the symmetric steady-state solution, and consequently $b = \text{tr}J_e$, depends on l_1/l_0 and L/l_0 . In contrast, the stability properties of this solution, as to be analyzed from (3.7) below in §3.1, depends on l_1/l_0 , L/l_0 , and $\tau_v \equiv 1/\sigma_v$.

In our stability analysis we will consider two distinct cases. In §3.1 we analyze (3.7) in the limit $\epsilon \rightarrow 0$ where the membrane-bulk leakage parameter satisfies $k_v = \mathcal{O}(\epsilon)$, so that $\beta = \mathcal{O}(1)$ in (3.5). For the parameter values given in [9]

$$(3.10 a) \quad D_v = 0.5, \quad \epsilon = 0.015, \quad \sigma_v = D_v/100, \quad z = 3.5, \quad q = 5, \quad L = 10, \quad k_v = 0.0225,$$

we calculate that

$$(3.10 b) \quad l_1 = 1.5, \quad l_0 = 10, \quad \tau_v = 200, \quad \frac{l_1}{l_0} = 0.15, \quad \frac{L}{l_0} = 1.$$

For this parameter set, our small ϵ stability analysis below will provide a theoretical understanding of the numerical results in [9]. In §3.2, we use a numerical winding number approach together with numerically computed global bifurcation diagrams, obtained using the bifurcation software XPPAUT [7], to study the $\epsilon = \mathcal{O}(1)$ problem.

3.1 Stability Analysis for the $\epsilon \rightarrow 0$ Limiting Problem

In this subsection we study the roots of (3.7) for various ranges of b . To determine the winding number $[\arg \mathcal{G}_{\pm}^0]_{\Gamma_+}$ in (3.9) we must consider several distinct ranges of λ_I . For $\epsilon \ll 1$, we will calculate this winding number analytically.

We first observe that $\text{Re}(\mathcal{G}_{\pm}^0(i\lambda_I)) \rightarrow l_0/l_1 > 0$ as $\lambda_I \rightarrow +\infty$, so that in the $(\mathcal{G}_{R\pm}^0, \mathcal{G}_{I\pm}^0)$ plane, where $\mathcal{G}_{R\pm}^0(\lambda_I) \equiv \text{Re}(\mathcal{G}_{\pm}^0(i\lambda_I))$ and $\mathcal{G}_{I\pm}^0(\lambda_I) \equiv \text{Im}(\mathcal{G}_{\pm}^0(i\lambda_I))$, we begin at a point on the positive real axis. Then, since $\text{Re}(\sqrt{1 + \tau_v \lambda}) > 0$, and both $\text{Re}(\tanh z) > 0$ and $\text{Re}(\coth z) > 0$ when $\text{Re}(z) > 0$, we conclude for $\epsilon \rightarrow 0$ from (3.7) that $\mathcal{G}_{R\pm}^0(\lambda_I) > 0$ for $\lambda_I > 0$ with $\lambda_I = \mathcal{O}(1)$. We then use (3.7) to calculate $\mathcal{G}_{\pm}^0(0)$, for any $\epsilon > 0$, as

$$(3.11) \quad \mathcal{G}_{\pm}^0(0) = \frac{l_0}{l_1 q_{\pm}(0)} - \frac{(b + \epsilon)}{a}, \quad \text{where} \quad a = z - \epsilon - b > 0.$$

We conclude that $\mathcal{G}_{\pm}^0(0) > 0$ when $b + \epsilon < a l_0 / [l_1 q_{\pm}(0)]$. Since $a = z - \epsilon - b > 0$, we solve this inequality for b to obtain that $\mathcal{G}_{\pm}^0(0) > 0$ when $b < b_{\pm}$ and $\mathcal{G}_{\pm}^0(0) < 0$ when $b > b_{\pm}$, where b_{\pm} is defined by

$$(3.12) \quad b < b_{\pm} \equiv z \left[1 + \frac{l_1 q_{\pm}(0)}{l_0} \right]^{-1} - \epsilon.$$

For the synchronous (+) mode, we now show that $b < b_+$ always holds for any root to the cubic $\mathcal{H}(u) = 0$, defined in (3.3). In particular, we will prove that $b > b_+$ is incompatible with a root of (3.3). To show this, we first observe that since $q_+(0) = \tanh(L/2l_0)$, the condition $b > b_+$ is equivalent to $b > \beta - \epsilon$, where β is defined in (3.5). We have from (3.6) that $b > \beta - \epsilon$ and $\beta > 0$, when $0 < \beta < 1 - 3q(u-2)^2$, where $u > 0$ is the unique root of $\mathcal{H}(u) \equiv q(u-2)^3 + \beta u - (4+u) = 0$. From this inequality on β , we calculate

$$\mathcal{H}(u) < q(u-2)^3 + u [1 - 3q(u-2)^2] - (4+u) = q(u-2)^3 - 4 - 3qu(u-2)^2 = -2q(u-2)^2(u+1) - 4 < 0,$$

for all $u > 0$. Therefore, there is no root to $\mathcal{H}(u) = 0$ when $b > b_+$. As a consequence, we must have $b < b_+$, so that for the synchronous mode we have $\mathcal{G}_+^0(0) > 0$ unconditionally.

To determine the curve in the l_1/l_0 versus L/l_0 plane where the asynchronous (-) mode has a zero-eigenvalue crossing, we set $b = b_-$, and use (3.12) together with (3.3) to obtain that a zero eigenvalue crossing occurs when

$$z \left[1 + \frac{l_1}{l_0} \tanh\left(\frac{L}{2l_0}\right) \right]^{-1} = -\frac{q(u-2)^3}{u} + \frac{4}{u} + 1, \quad z \left[1 + \frac{l_1}{l_0} \coth\left(\frac{L}{2l_0}\right) \right]^{-1} = 1 - 3q(u-2)^2.$$

We rearrange these expressions to get

$$(3.13) \quad \begin{aligned} \frac{l_1}{l_0} \tanh\left(\frac{L}{2l_0}\right) &= \chi_1(u), & \chi_1(u) &\equiv \frac{zu}{-q(u-2)^3 + 4 + u} - 1, \\ \frac{l_1}{l_0} \coth\left(\frac{L}{2l_0}\right) &= \chi_2(u), & \chi_2(u) &\equiv \frac{zu}{1 - 3q(u-2)^2} - 1. \end{aligned}$$

For the range of $u > 0$ for which $\chi_1 > 0$, $\chi_2 > 0$, and $\chi_1/\chi_2 < 1$, we readily derive from (3.13) that the curve in the l_1/l_0 versus L/l_0 plane where the asynchronous (-) mode has a zero-eigenvalue crossing is given parametrically in terms of u by

$$(3.14) \quad \frac{l_1}{l_0} = \sqrt{\chi_1(u)\chi_2(u)}, \quad \frac{L}{l_0} = \ln\left(\frac{\sqrt{\chi_2(u)} + \sqrt{\chi_1(u)}}{\sqrt{\chi_2(u)} - \sqrt{\chi_1(u)}}\right).$$

For $q = 5$, $z = 3.5$, (3.14) yields the upward facing horseshoe-shaped curve shown in the left panel of Fig. 6. Below in (3.30), we show that this zero-eigenvalue crossing for the asynchronous mode is a bifurcation point where asymmetric equilibria of (3.1) bifurcate from the symmetric steady-state solution branch.

Now that the possibility of zero-eigenvalue crossings has been analyzed, we proceed to determine $[\arg \mathcal{G}_{\pm}^0]_{\Gamma_{\pm}}$. Since $\mathcal{G}_{R\pm}^0(\lambda_I) > 0$ for $\lambda_I > 0$ with $\lambda_I = \mathcal{O}(1)$, we need only analyze (3.7) with $\lambda = i\lambda_I$ and λ_I near the origin. For $|b| \gg \mathcal{O}(\epsilon)$, we set $\lambda_I = \epsilon \lambda_I^0$ with $\lambda_I^0 = \mathcal{O}(1)$ in (3.7) to obtain

$$(3.15) \quad \mathcal{G}_{R\pm}^0 = \text{Re}(\mathcal{G}_{\pm}^0(i\epsilon \lambda_I^0)) \sim \frac{l_0}{l_1 q_{\pm}(0)} - \frac{ba}{a^2 + b^2(\lambda_I^0)^2}.$$

For the synchronous mode, we conclude from (3.15) that $\mathcal{G}_{R\pm}^0 > 0$ when $\lambda_I = \mathcal{O}(\epsilon)$, and consequently $[\arg \mathcal{G}_{I\pm}^0]_{\Gamma_+} = 0$, for any b with $|b| \gg \mathcal{O}(\epsilon)$. As a result, for the synchronous mode, we obtain from (3.9) that

$$(3.16) \quad N = P, \quad \text{where} \quad P = \begin{cases} 2 & \text{if } b = \text{tr} J_e > 0 \\ 0 & \text{if } b = \text{tr} J_e < 0 \end{cases}, \quad (\text{synchronous mode}).$$

In contrast, for the asynchronous mode, we conclude from (3.15) that for $\lambda_I = \mathcal{O}(\epsilon)$ and $|b| \gg \mathcal{O}(\epsilon)$, we have $\mathcal{G}_{R-}^0(\lambda_I) > 0$ when $b < b_-$, and $\mathcal{G}_{R-}^0(\lambda_I) < 0$ when $b > b_-$, where b_- is defined in (3.12). Therefore, for the asynchronous mode, we have $[\arg \mathcal{G}_{I\pm}^0]_{\Gamma_+} = 0$ when $b < b_-$, so that (3.16) still holds when $b < b_-$ and $|b| \gg \mathcal{O}(\epsilon)$. However, it remains to calculate $[\arg \mathcal{G}_{I\pm}^0]_{\Gamma_+} = 0$ when $b > b_-$, for which $\mathcal{G}_{R-}^0(\lambda_I) < 0$. This computation is done numerically below.

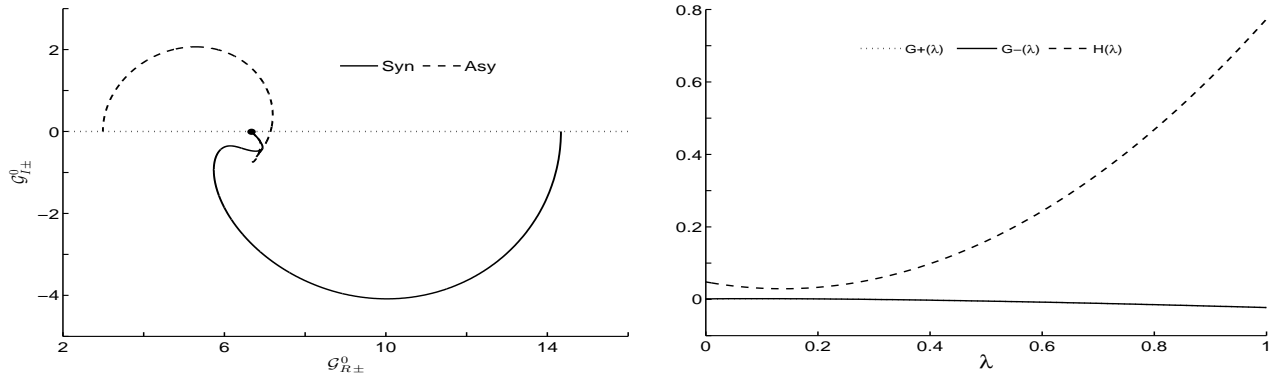


Figure 5. Left panel: The path $\mathcal{G}_{\pm}^0(i\lambda_I) = \mathcal{G}_{R\pm}^0(\lambda_I) + i\mathcal{G}_{I\pm}^0(\lambda_I)$, for the parameter set (3.10 *a*) of [9]. For both \pm modes, we start at $\lambda_I = 100$ (solid dot), which corresponds to the common value $\mathcal{G}_{R\pm}^0 \sim l_0/l_1 > 0$ and $\mathcal{G}_{I\pm}^0 = 0$. As λ_I increases, $\mathcal{G}_{R\pm}^0$ remains positive, and the path for each mode terminates when $\lambda_I = 0$ at different points on the positive real axis, without wrapping around the origin. This establishes that $[\arg \mathcal{G}_{I\pm}^0]_{\Gamma_+} = 0$. Right panel: The functions $G_{\pm}(\lambda)$ and $H(\lambda)$, as defined in (3.17), when $\lambda > 0$ is real, for the parameter set (3.10 *a*). The curves for G_+ and G_- essentially coincide. Since there are no intersections between G_{\pm} and $H(\lambda)$, then there are no real positive roots to $\mathcal{G}_{\pm}^0(\lambda) = 0$ in (3.7) for either the synchronous or asynchronous modes.

For any b independent of ϵ , this analysis shows for the synchronous mode that $N = 0$ for $b < 0$ and $N = 2$ for any $b > 0$. For the asynchronous mode we have $N = 0$ for $b < 0$ and $N = 2$ for any $0 < b < b_-$. As a result, to leading order in ϵ , we conclude that both the synchronous and asynchronous modes undergo a Hopf bifurcation as b crosses through zero. For the parameter set (3.10 *a*), as used in [9], in the left panel of Fig. 5 we plot the numerically computed path of $\mathcal{G}_{\pm}^0(i\lambda_I)$ in the plane $(\mathcal{G}_{R\pm}^0, \mathcal{G}_{I\pm}^0)$. For this parameter set we calculate numerically that $b_- \approx 2.627$ and $b_+ \approx 3.258$ from (3.12), and $b = \text{tr} J_e = 1 - \epsilon - 3q(u_e - 2)^2 \approx 0.2746$, from (2.18), where u_e is the unique root of $\mathcal{H}(u) = 0$ defined in (3.3). Since $b < b_-$, our theoretical prediction that $[\arg \mathcal{G}_{I\pm}^0]_{\Gamma_+} = 0$ is confirmed from the plot in the left panel of Fig. 5.

To determine the location of the two unstable eigenvalues of the linearization for the parameter set of (3.10 *a*), we look for zeroes of (3.7) on the positive real axis $\lambda > 0$. To this end, we rewrite (3.7) as

$$(3.17) \quad \mathcal{G}_{\pm}^0(\lambda) = \frac{H(\lambda) - G_{\pm}(\lambda)}{\left[\frac{l_{\pm}}{l_0} H(\lambda) q_{\pm}(\tau_v \lambda) \right]}, \quad H(\lambda) \equiv \lambda^2 - b\lambda + \epsilon a, \quad G_{\pm}(\lambda) \equiv \frac{\epsilon l_1}{l_0} (b + \epsilon - \lambda) q_{\pm}(\tau_v \lambda) \sqrt{1 + \tau_v \lambda}.$$

For the parameter set of (3.10 *a*), in the right panel of Fig. 5 we plot $G_{\pm}(\lambda)$ and $H(\lambda)$ for $\lambda > 0$ real, which shows that there are no real positive roots to $\mathcal{G}_{\pm}^0(\lambda) = 0$. As a result, the two unstable eigenvalues for the parameter set (3.10 *a*) are not real-valued, and do indeed generate an oscillatory instability of the symmetric steady-state solution.

Next, we examine the region near $b = 0$ where a Hopf bifurcation for either of the two modes must occur. To determine

the precise location of the Hopf bifurcation point we look for a root λ_I of (3.7), with $\lambda_I \ll 1$, when $b = \mathcal{O}(\epsilon)$. We Taylor-expand the right-hand side of (3.7) as $\lambda_I \rightarrow 0$, and set $\mathcal{G}_\pm^0(i\lambda_I) = 0$ to obtain that

$$(3.18) \quad -\lambda_I^2 - ib\lambda_I + \epsilon(z - \epsilon - b) \sim \epsilon(c_\pm + i\lambda_I s_\pm + \mathcal{O}(\lambda_I^2)) \left(1 + \frac{i}{2}\tau_v\lambda_I + \mathcal{O}(\lambda_I^2)\right) (b + \epsilon - i\lambda_I),$$

where c_\pm and s_\pm are determined from the Taylor series of $l_1 q_\pm(i\tau_v\lambda_I)/l_0$ as

$$(3.19) \quad \frac{l_1}{l_0} q_\pm(i\tau_v\lambda_I) = c_\pm + i\lambda_I s_\pm + \mathcal{O}(\lambda_I^2); \quad c_\pm \equiv \frac{l_1}{l_0} q_\pm(0), \quad s_\pm \equiv \frac{l_1}{l_0} \tau_v q'_\pm(0).$$

Upon expanding the right-hand side of (3.18), we obtain that

$$(3.20) \quad -\lambda_I^2 - ib\lambda_I + \epsilon(z - \epsilon - b) \sim \epsilon \left[c_\pm + i \left(s_\pm + \frac{c_\pm}{2} \tau_v \right) \lambda_I + \mathcal{O}(\lambda_I^2) \right] (b + \epsilon - i\lambda_I).$$

To determine λ_I and the critical value of b for a Hopf bifurcation we take the real and imaginary parts of both sides of (3.20). From the imaginary parts, we get $b \sim \epsilon c_\pm - \epsilon(b + \epsilon)(s_\pm + c_\pm \tau_v/2)$. Upon solving for b , we obtain that

$$(3.21) \quad b \sim \epsilon c_\pm - \epsilon^2(c_\pm + 1) \left(s_\pm + \frac{c_\pm}{2} \tau_v \right).$$

Next, by taking the real parts of both sides of (3.18), we get

$$-\lambda_I^2 + \epsilon(z - \epsilon - b) \sim \epsilon(b + \epsilon)c_\pm + \epsilon\lambda_I^2 \left(s_\pm + \frac{c_\pm}{2} \tau_v \right).$$

We substitute $b \sim \epsilon c_\pm$ into this equation, and simplify the resulting expression to get

$$\lambda_I^2 \sim \epsilon z - \epsilon^2(c_\pm + 1)^2 - \epsilon\lambda_I^2 \left(s_\pm + \frac{c_\pm}{2} \tau_v \right).$$

For $\epsilon \ll 1$, we readily derive from this last expression that

$$(3.22 a) \quad \lambda_I \sim \epsilon^{1/2} z^{1/2} \left(1 - \frac{\epsilon}{2z} \left[(c_\pm + 1)^2 + z \left(s_\pm + \frac{c_\pm}{2} \tau_v \right) \right] \right) + \mathcal{O}(\epsilon^2).$$

Upon recalling (3.19) and (3.8), we determine c_\pm and s_\pm as

$$(3.22 b) \quad c_\pm = \begin{cases} \frac{l_1}{l_0} \tanh\left(\frac{L}{2l_0}\right), & \text{synchronous (+)} \\ \frac{l_1}{l_0} \coth\left(\frac{L}{2l_0}\right), & \text{asynchronous (-)} \end{cases}, \quad s_\pm = \begin{cases} \frac{\tau_v}{4} \left(\frac{l_1}{l_0}\right) \left(\frac{L}{l_0}\right) \operatorname{sech}^2\left(\frac{L}{2l_0}\right), & \text{synchronous (+)} \\ -\frac{\tau_v}{4} \left(\frac{l_1}{l_0}\right) \left(\frac{L}{l_0}\right) \operatorname{csch}^2\left(\frac{L}{2l_0}\right), & \text{asynchronous (-)} \end{cases}.$$

In summary, we conclude to leading-order in the limit $\epsilon \rightarrow 0$ that there is a Hopf bifurcation when $b \equiv \operatorname{tr}J_e \sim \epsilon c_\pm$ with leading-order frequency $\lambda_I \sim \epsilon^{1/2} z^{1/2}$. Therefore, the period T of small-amplitude oscillations at the onset of the Hopf bifurcation is long as $\epsilon \rightarrow 0$, with scaling $T \sim 2\pi/\sqrt{\epsilon z}$. A higher-order asymptotic formulae for the Hopf point is given in (3.21) and (3.22). The critical threshold for b , given by $b \sim \epsilon c_\pm$, shows that the Hopf bifurcation threshold for the synchronous and asynchronous modes are only slightly different when $\epsilon \ll 1$.

To determine the curves in the l_1/l_0 versus L/l_0 parameter plane where Hopf Bifurcations occur, we set $b = \operatorname{tr}J_e = 1 - \epsilon - 3q(u_e - 2)^2 = \epsilon c_\pm$, and solve for u_e . This yields the two roots $u_{1\pm}$ and $u_{2\pm}$, defined by

$$(3.23) \quad u_{1\pm} = 2 - \frac{1}{\sqrt{3q}} \sqrt{1 - \epsilon(1 + c_\pm)}, \quad u_{2\pm} = 2 + \frac{1}{\sqrt{3q}} \sqrt{1 - \epsilon(1 + c_\pm)}.$$

By using (3.3), we then solve $\mathcal{H}(u_{1\pm}) = 0$ and $\mathcal{H}(u_{2\pm}) = 0$ for β to obtain that $\beta = Z(u_{1\pm})$ and $\beta = Z(u_{2\pm})$, where

$$(3.24) \quad Z(u) \equiv 1 + \frac{4}{u} - \frac{(1 - \epsilon)}{3u}(u - 2).$$

Finally, we use (3.5) to relate β to l_1/l_0 and L/l_0 . Upon solving the resulting expression for l_1/l_0 we obtain that the Hopf

bifurcation curves for the synchronous and asynchronous modes are given by

$$(3.25 a) \quad \frac{l_1}{l_0} = \left[\frac{z}{Z(u_{j+})} - 1 \right] \coth \left(\frac{L}{2l_0} \right), \quad \text{for } j = 1, 2; \quad \text{synchronous (+) mode,}$$

$$(3.25 b) \quad \frac{l_1}{l_0} = \left[\frac{z}{Z(u_{j-})} - 1 \right] \coth \left(\frac{L}{2l_0} \right), \quad \text{for } j = 1, 2; \quad \text{asynchronous (-) mode,}$$

where $Z(u)$ is defined in (3.24) and c_{\pm} is defined in (3.22 b). We remark that since c_{\pm} depends on l_1/l_0 , (3.25) is a weakly implicit equation for l_1/l_0 when $\epsilon \ll 1$. We solve (3.25) when $\epsilon \ll 1$ for l_1/l_0 using one step of a fixed point iteration.

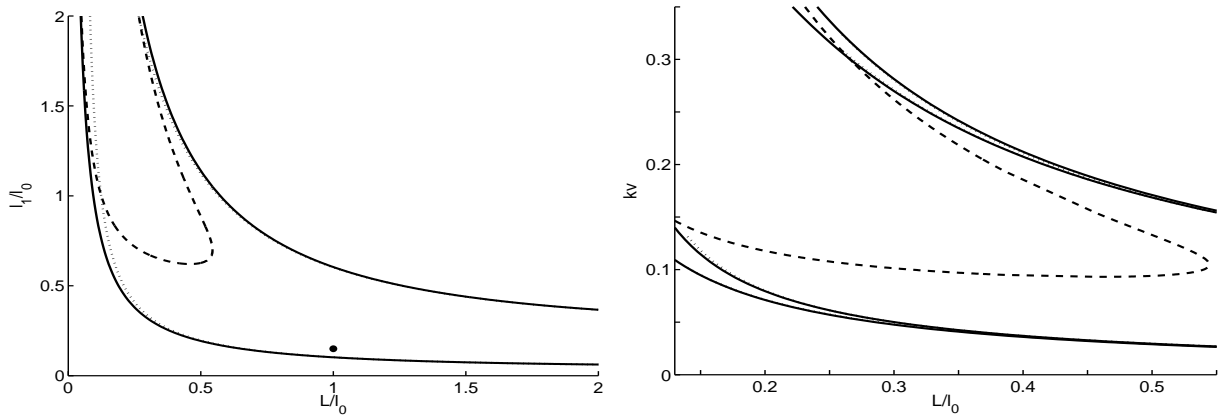


Figure 6. Left panel: The Hopf bifurcation boundaries for the synchronous mode (solid curves) and asynchronous mode (dotted curves), as computed from (3.25), for the one-bulk species model (3.1) when $q = 5$, $z = 3.5$, $\tau_v = 200$, and $\epsilon = 0.015$. These Hopf bifurcation thresholds essentially coincide except when L/l_0 is small. The upward horseshoe-shaped curve corresponds to a zero-eigenvalue crossing for the asynchronous mode, as given parametrically by (3.14). The marked point corresponds to the parameter set $l_1/l_0 = 0.15$ and $L/l_0 = 1$ used in [9]. Right panel: Phase diagram in the k_v versus L/l_0 plane when $l_0 = 10$ showing a clear difference between the Hopf bifurcation boundaries for the synchronous (outer solid) and asynchronous (inner solid) curves. Between the two outer solid curves, the synchronous mode is unstable while between the inner solid curves the asynchronous mode is unstable. The dashed horseshoe shaped-curve corresponds to the zero eigenvalue crossing (3.14). Inside the region bounded by horseshoe-shaped curve there are asymmetric steady-state solutions. The Hopf curves coincide almost exactly with full numerical results computed by solving (3.4) for a pure imaginary eigenvalue $\lambda = i\omega$ using Maple [19] (dotted curve).

In the left panel of Fig. 6 we plot the Hopf bifurcation curves from (3.25) in the l_1/l_0 versus L/l_0 plane when $\epsilon = 0.015$, $q = 5$, and $z = 3.5$. For this parameter set, we observe from this figure that the Hopf bifurcation thresholds for the synchronous and asynchronous modes almost coincide. Inside the region bounded by the curves, the symmetric steady-state solution is unstable and there may either be stable or unstable periodic solutions. The parameter set (3.10 a), as used in [9], corresponds to the marked point $l_1/l_0 = 0.15$ and $L/l_0 = 1$ in this figure that is near the stability boundary. This phase diagram is comparable to the one obtained in [9]. However, as discussed in §1, in [9] the Hopf bifurcation boundary for the leading order theory, where the synchronous and asynchronous modes have a common threshold, was obtained qualitatively through an analysis based on the crossing of nullclines. No zero-eigenvalue crossing was noted in [9]. Our stability analysis for the limiting problem $\epsilon \rightarrow 0$ has been able to determine two-term approximations to the Hopf boundaries for both the synchronous and asynchronous modes, to determine the Hopf bifurcation frequencies near onset, and to detect zero-eigenvalue crossings corresponding to the emergence of asymmetric steady-state solutions of (3.1).

In the right panel of Fig. 6 we plot the corresponding Hopf bifurcation curves in the k_v versus L/l_0 when $l_0 = 10$, which shows a clearer distinction between the synchronous and asynchronous modes of instability. Between the two outer

solid curves, representing the Hopf threshold for the synchronous mode, the synchronous mode is unstable. Similarly, between the two inner solid curves, representing the Hopf threshold for the asynchronous mode, the asynchronous mode is unstable. The dashed horseshoe-shaped curve corresponds to a zero eigenvalue crossing. Inside this horseshoe-shaped region, there are asymmetric steady-state solutions to (3.1). This plot shows that for a given value of L/l_0 the symmetric steady-state solution is unstable to an oscillatory instability only for some intermediate range $k_{v-} < k_v < k_{v+}$ of the leakage parameter, which couples the membrane and the bulk. We remark that the analytical stability boundaries in Fig. 6 were all verified numerically by determining the complex roots of $\mathcal{G}_{\pm} = 0$, as defined in (3.4), using Maple [19].

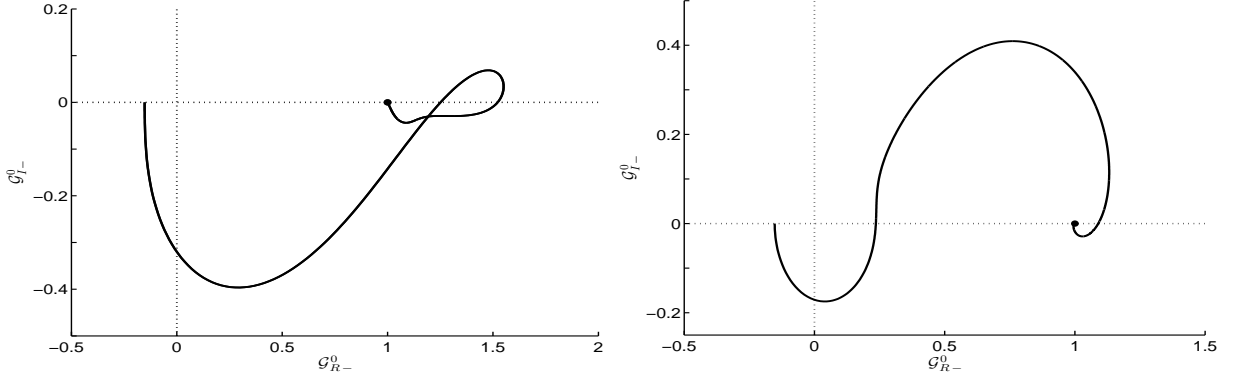


Figure 7. Plot of $\mathcal{G}_{-}^0(i\lambda_I) = \mathcal{G}_{R-}^0(\lambda_I) + i\mathcal{G}_{I-}^0(\lambda_I)$ for the parameter set $l_1/l_0 = 1.0$, $L/l_0 = 0.4$, $q = 5.0$, $z = 3.5$, that lies within the horseshoe-shaped region of the left panel of Fig. 6 where $b > b_-$. Left panel: $\tau_v = 200$. Right panel: $\tau_v = 1$. For $\lambda_I \rightarrow \infty$, both paths begin on the positive real axis, and end on the negative real axis when $\lambda_I = 0$. For both values of τ_v we have $[\arg \mathcal{G}_{-}^0]_{\Gamma_+} = -\pi$, so that $N = 1$ from (3.9).

Next, we numerically compute the winding number $[\arg \mathcal{G}_{-}^0]_{\Gamma_+}$ to count the number of unstable eigenvalues for the asynchronous mode for parameter values inside the horseshoe-shaped zero-eigenvalue crossing curve in the left panel of Fig. 6. Recall that within this region, we have $b > b_-$ and so $\mathcal{G}_{-}^0(0) < 0$. For the particular point $l_1/l_0 = 1.0$ and $L/l_0 = 0.4$ in this region, and for $q = 5$ and $z = 3.5$, in Fig. 7 we show that $[\arg \mathcal{G}_{-}^0]_{\Gamma_+} = -\pi$ for two different values of τ_v . From (3.9) this implies that $N = 1$, and so for the asynchronous mode the linearization around the symmetric steady-state has a unique unstable real eigenvalue. By further similar numerical computations of the winding number (not shown), we conjecture that $[\arg \mathcal{G}_{-}^0]_{\Gamma_+} = -\pi$, and consequently $N = 1$ for the asynchronous mode, whenever $b > b_-$.

In the left panel of Fig. 8 we show the numerically computed spectrum of the linearization, obtained using Maple [19] on (3.7), for a vertical slice at fixed $L/l_0 = 0.3$ in the right panel of Fig. 6 that begins within the horseshoe-shaped region, first traversing above the zero-eigenvalue curve, then past the asynchronous Hopf threshold, and finally beyond the synchronous Hopf threshold. A zoom of the region in Fig. 6 where these crossings are undertaken is shown in the right panel of Fig. 8. The transition in the spectrum as predicted by our theory is confirmed (see the caption of Fig. 8).

Next, we show analytically that the zero-eigenvalue crossing for the asynchronous mode at $b = b_-$ corresponds to a bifurcation point where asymmetric equilibria of (3.1) bifurcate from the symmetric steady-state solution branch. To show this, we first construct a more general steady-state solution (3.1), where we remove the symmetry assumption about the midline $x = L/2$. For this more general steady-state, we calculate from the steady-state system for (3.1) that

$$(3.26) \quad V_e(x) = v_1 \frac{\sinh[\omega_v(L-x)]}{\sinh(\omega_v L)} + v_2 \frac{\sinh(\omega_v x)}{\sinh(\omega_v L)}, \quad \omega_v \equiv \sqrt{\sigma_v/D_v},$$

where $v_1 = V_e(0)$ and $v_2 = V_e(L)$. By setting $\epsilon g(u_1, v_1) + k_v V_{ex}(0) = 0$ and $\epsilon g(u_2, v_2) - k_v V_{ex}(L) = 0$, we readily derive,

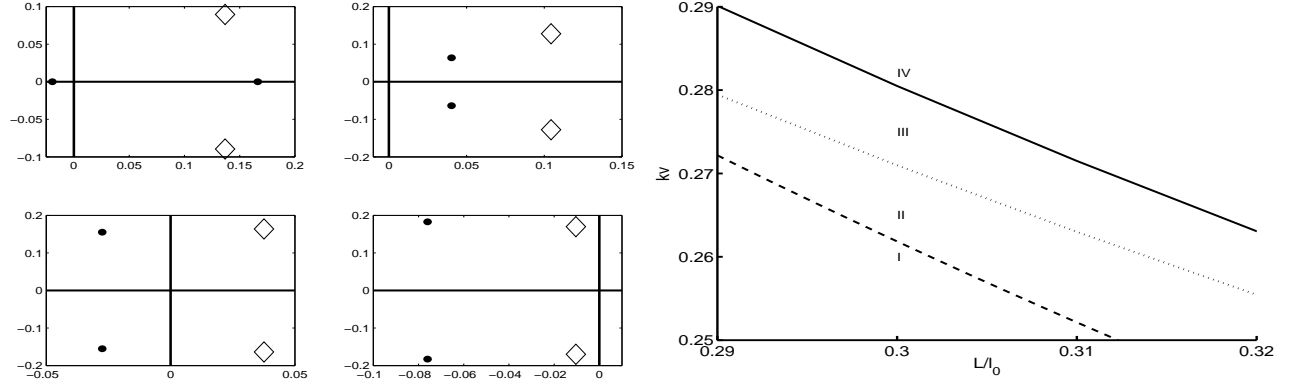


Figure 8. The spectrum $\text{Im}(\lambda)$ versus $\text{Re}(\lambda)$ (left panel) near the origin for the asynchronous (solid dots) and synchronous (diamonds) modes for a fixed $L/l_0 = 0.3$, $l_0 = 10$, $q = 5$, $z = 3.5$, $\tau_v = 200$, and $\epsilon = 0.015$, as the leakage k_v crosses various stability boundaries as shown in the right panel, representing a zoom of a portion of the k_v versus L/l_0 plane of the right panel of Fig. 6. The stability boundaries in this figure are obtained using Maple [19] on (3.7). The subplots in the left figure are as follows: Top left $k_v = 0.26$ (in the horseshoe-shaped region I): $N = 1$ and $N = 2$ for the anti-phase and in-phase modes, respectively. Top right: $k_v = 0.265$ (outside the horseshoe, but before the asynchronous Hopf boundary: region II): $N = 2$ for both anti-phase and in-phase modes. Bottom Left: $k_v = 0.275$ (between the asynchronous and synchronous Hopf boundaries: region III): $N = 0$ for the anti-phase and $N = 2$ for the in-phase modes. Bottom Right: $k_v = 0.282$ (above the synchronous Hopf boundary: region IV): $N = 0$ for both the anti-phase and in-phase modes. These spectral results are all consistent with our stability theory.

in terms of a 2×2 symmetric matrix \mathcal{A} , that

$$(3.27 a) \quad \mathcal{A} \begin{pmatrix} v_1 \\ v_2 \end{pmatrix} = z \begin{pmatrix} u_1 \\ u_2 \end{pmatrix}, \quad \mathcal{A} \equiv \begin{pmatrix} 1 + \frac{l_1}{l_0} \coth\left(\frac{L}{l_0}\right) & -\frac{l_1}{l_0} \text{csch}\left(\frac{L}{l_0}\right) \\ -\frac{l_1}{l_0} \text{csch}\left(\frac{L}{l_0}\right) & 1 + \frac{l_1}{l_0} \coth\left(\frac{L}{l_0}\right) \end{pmatrix}.$$

Upon setting $f(u_j, v_j) = 0$, $j = 1, 2$, we obtain a nonlinear algebraic system for $\mathbf{u} \equiv (u_1, u_2)^T$ given by $\mathcal{N}(\mathbf{u}) = 0$, where

$$(3.27 b) \quad \mathcal{N}(\mathbf{u}) \equiv -q \begin{pmatrix} (u_1 - 2)^3 \\ (u_2 - 2)^3 \end{pmatrix} + 4 \begin{pmatrix} 1 \\ 1 \end{pmatrix} + \mathbf{u} - z\mathcal{A}^{-1}\mathbf{u}.$$

Since the matrix \mathcal{A} is symmetric and has a constant row sum, it follows that $\mathbf{q}_1 \equiv (1, 1)^T$ (in-phase) and $\mathbf{q}_2 \equiv (1, -1)^T$ (anti-phase) are its two eigenvectors. After some algebra, we obtain that the two corresponding eigenvalues are

$$(3.28) \quad \mathcal{A}\mathbf{q}_j = \mu_j \mathbf{q}_j; \quad \mu_1 = 1 + \frac{l_1}{l_0} \tanh\left(\frac{L}{2l_0}\right), \quad \mu_2 = 1 + \frac{l_1}{l_0} \coth\left(\frac{L}{2l_0}\right).$$

To recover the construction of the symmetric steady-state branch we use $\mathbf{q}_1 \equiv (1, 1)^T$, and look for a solution to (3.27 b) with $u_1 = u_2 \equiv u_e$. Since $z\mathcal{A}^{-1}\mathbf{q}_1 = z\mu_1^{-1}\mathbf{q}_1$, and $z\mu_1^{-1} = \beta$, we readily identify that (3.27 b) reduces to (3.3), where β is defined in (3.5). To determine whether there are any bifurcation points from this symmetric branch, we write $\mathbf{u} = u_e(1, 1)^T + \delta\phi$, where $\delta \ll 1$ and ϕ is a 2-vector. Upon linearizing (3.27 b), we readily obtain that

$$(3.29) \quad \mathcal{A}\phi = \left(\frac{z}{1 - 3q(u_e - 2)^2} \right) \phi.$$

Bifurcation points correspond to where (3.29) has a nontrivial solution. Such points occur whenever

$$(3.30) \quad 1 - 3q(u_e - 2)^2 = \beta, \quad (\text{in-phase}); \quad 1 - 3q(u_e - 2)^2 = z \left[1 + \frac{l_1}{l_0} \coth\left(\frac{L}{2l_0}\right) \right]^{-1}, \quad (\text{anti-phase}).$$

As shown previously, the in-phase equation above is inconsistent with any root of the cubic (3.3). In contrast, the anti-

phase equation in (3.30) is precisely the condition $b = b_-$. Therefore, zero eigenvalue crossings for the asynchronous mode correspond to where branches of asymmetric steady-state solutions bifurcate from the symmetric steady-state branch.

In the left panel of Fig. 9 we plot a global bifurcation diagram versus the leakage parameter k_v showing only the symmetric and asymmetric steady-state solution branches and the two bifurcation points off of the symmetric branch. This plot corresponds to taking a slice at fixed L/l_0 through the phase diagram in the right panel of Fig. 6. It also corresponds to the solution set of the nonlinear algebraic system (3.27 b). Although the bifurcation diagram can be obtained from (3.27 b), we used the numerical bifurcation software XPPAUT [7] after first discretizing (3.1) into a large set of ODE's. In this way, the stability properties of the asymmetric steady-state branch was determined numerically. Our computations show that the asymmetric solution branch is unstable except in a narrow window of k_v . In the right panel of Fig. 9 we show results from full numerical solutions to the PDE-ODE system (3.1), computed using a method of lines approach, that verify this prediction of a stable window in k_v for the stability of the asymmetric steady-state solutions.

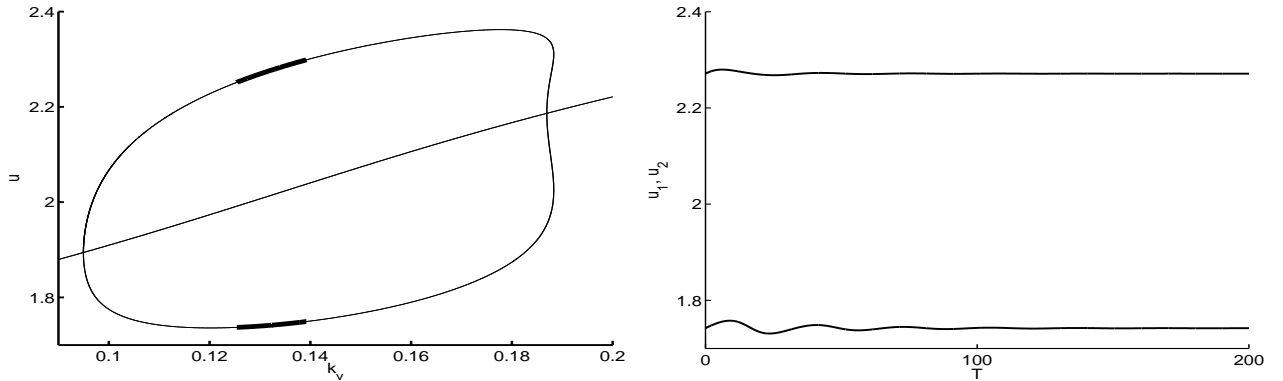


Figure 9. Left panel: Global bifurcation diagram of u_1 and u_2 , computed using XPPAUT [7], for the asymmetric and symmetric steady-state solutions to (3.1) showing the two bifurcation points off of the symmetric steady-state branch. The parameter values are $l_0 = 10$, $L/l_0 = 0.4$, $q = 5$, $z = 3.5$, $\tau_v = 200$, and $\epsilon = 0.015$. Thin curves represent unstable steady-state solutions while thick curves indicate stable ones. Right panel: Time evolution of u_1 , u_2 , as computed from the full PDE-ODE system (3.1) using a method of lines approach. The parameter values are in left panel except that $k_v = 0.13$ is chosen so that the asymmetric steady-state solution is stable. Initial conditions for (3.1) are chosen close to the stable asymmetric solution. As expected, the two u_i approach their steady-state values after a transient period.

In the left panel of Fig. 10, we plot a global bifurcation diagram of u_1 versus k_v , computed using XPPAUT [7], showing only the local branching behavior of the synchronous periodic solution branch near the Hopf bifurcation point where it emerges from the symmetric steady-state branch. In the right panel of Fig. 10 we plot the corresponding period of the synchronous oscillations. The periodic solution branch is found to be supercritical at onset, with a narrow range of k_v where the branch is unstable. Stability is regained at some larger value of k_v . From the right panel of Fig. 10 the period of oscillations at onset is 27.99, which agrees rather well with the asymptotic result $T = 2\pi/\lambda_I \approx 30.42$, where we used $\lambda_I \approx 0.2065$ as computed from (3.22 a) for the synchronous mode.

Finally, to illustrate the oscillatory dynamics, full time-dependent numerical solutions for $V(x, t)$ from the coupled PDE-ODE system (3.1) were computed using a method of lines approach. We choose three parameter sets that are inside the region of the left panel of Fig. 6 where both oscillatory modes are unstable with $N = 2$ unstable eigenvalues for each mode. In the left and middle panels in Fig. 11, representing contour plots of $V(x, t)$, we show the clear possibility of either stable synchronous or stable asynchronous oscillatory instabilities, depending on the particular point chosen within the instability region. For the right panel in Fig. 11, we use the parameter set (3.10 a) of [9], for which $k_v = 0.0225$, which

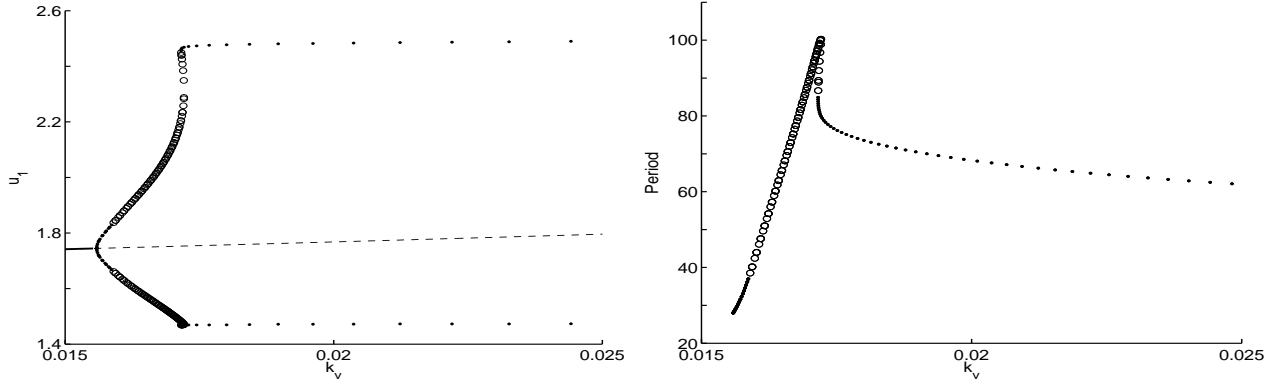


Figure 10. Left panel: The global bifurcation diagram of u_1 versus k_v , computed using XPPAUT [7], for in-phase perturbations, showing the periodic solution branch of synchronous oscillations near the lower Hopf boundary for the synchronous mode in the right panel of Fig. 6. The other parameter values are $L/l_0 = 1.0$, $l_0 = 10$, $q = 5$, $z = 3.5$, $\tau_v = 200$, and $\epsilon = 0.015$ corresponding to the parameter set (3.10 a) of [9]. Right panel: The period of oscillations along the synchronous branch. The solid and open circles in both plots represent stable and unstable periodic solutions, respectively. The solid and dashed lines in the left panel are stable and unstable symmetric steady-state solutions, respectively.

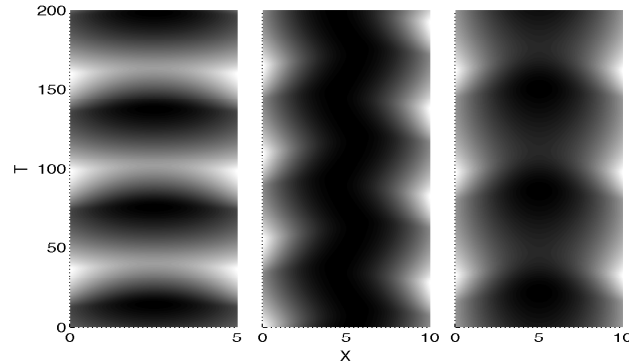


Figure 11. Full numerical simulations of the PDE-ODE system (3.1) for $V(x, t)$, with time running from bottom to top and space represented horizontally. The fixed parameter values are $q = 5$, $z = 3.5$, $\tau_v = 200$, and $\epsilon = 0.015$. The initial conditions used in the simulation are $V(x) = 0.5 = v_1 = v_2$, $u_1 = 1$, $u_2 = 5$. Left panel: $L = 5$ with $l_1/l_0 = 0.5$ and $L/l_0 = 0.5$ showing stable synchronous oscillations. Middle panel: $L = 10$ with $l_1/l_0 = 0.25$ and $L/l_0 = 1$ showing stable asynchronous oscillations. Right panel: $L = 10$ with $l_1/l_0 = 0.15$ and $L/l_0 = 1$ for the parameter set (3.10 a) of [9].

is close to the stability boundary where a Hopf bifurcation occurs (see the marked point in the left panel of Fig. 6). For this parameter set, we observe from the right panel of Fig. 10 that the synchronous periodic solution is stable and that the period of oscillations is $T \approx 64$. The corresponding full numerical results computed from the PDE-ODE system (3.1) shown in the right plot of Fig. 11 reveal stable synchronous oscillations with a period close to this predicted value.

Qualitatively, our results for the $\epsilon \ll 1$ regime show that when $L/l_0 = O(1)$, the in-phase and anti-phase Hopf bifurcation thresholds in terms of the leakage parameter k_v are asymptotically close, and that oscillatory instabilities only occur on some finite interval of k_v . However, when D_v/σ_v is large, or equivalently L is small, the parameter range of k_v where asynchronous instabilities occur is smaller than that for the corresponding synchronous range (see the right panel of Fig. 6). Moreover, our asymptotic calculation of the asymptotically long period of small amplitude oscillations on the boundaries in the phase diagram of Fig. 6 indicates that relaxation-type oscillations will occur near the Hopf point. Such oscillations are confirmed in the full numerical simulations shown in Fig. 11. Finally, our detailed analysis and use of the

winding-number criterion has revealed the existence of transcritical bifurcations to non-symmetric steady-state solutions that occurs at two distinct values of the leakage parameter only when D_v/σ_v exceeds a critical threshold, or equivalently when L is sufficiently small. These asymmetric equilibria are, however, typically unstable (see the left panel of Fig. 9), except on a narrow subinterval of the leakage k_v .

3.2 Stability Analysis for the $\epsilon = \mathcal{O}(1)$ Problem

Next, we study oscillatory dynamics for (3.1) when $\epsilon = 0.3$, which is a twenty-fold increase over the value used in §3.1. We use a combination of a numerical winding number computation, based on (3.9), to determine the stability properties of the symmetric steady-state, and Maple [19] to find the roots of (3.7) determining the eigenvalues of the linearization of (3.1) around the symmetric steady-state solution. Since for this larger value of ϵ the PDE-ODE system (3.1) is not as computationally stiff as when $\epsilon = 0.015$, we are able to use XPPAUT [7] to calculate global branches of synchronous and asynchronous periodic solutions. Asymmetric steady-state branches and their bifurcations are also computed.

In the left panel of Fig. 12 we plot the Hopf bifurcation curves, computed from the roots of (3.7), in the l_1/l_0 versus L/l_0 plane when $q = 5$, $z = 3.5$, $\tau_v = 200$, and $\epsilon = 0.3$. In contrast to the similar plot in the left panel of Fig. 6 where $\epsilon = 0.015$, we observe from the left panel of Fig. 12 that the Hopf bifurcation thresholds for the synchronous and asynchronous modes are now rather distinct when $L/l_0 < 0.5$. The left horseshoe-shaped curve is the zero-eigenvalue crossing boundary for the asynchronous mode, as parametrized by (3.14).

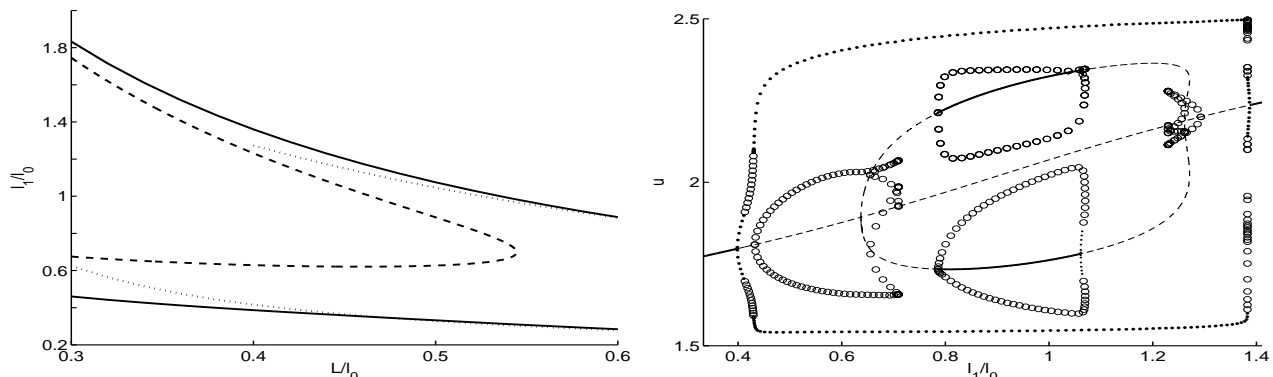


Figure 12. Left panel: The Hopf bifurcation boundaries for the synchronous (solid curves) and asynchronous (dotted curves) modes for the one-bulk species model (3.1), as computed from solving (3.7) with Maple [19] when $q = 5$, $z = 3.5$, $\tau_v = 200$, and $\epsilon = 0.3$. These Hopf bifurcation thresholds are distinct when $L/l_0 < 0.5$. The dashed curve is the zero-eigenvalue crossing for the asynchronous mode, given parametrically by (3.14). Right panel: Bifurcation diagram of u with respect to l_1/l_0 for a fixed $L/l_0 = 0.4$. The solid and dashed curves indicate stable and unstable steady-states, respectively. The solid and open circles correspond to stable and unstable periodic solutions, respectively. The synchronous and asynchronous periodic solution branches first bifurcate from the symmetric steady-state at $l_1/l_0 \approx 0.38$ and $l_1/l_0 \approx 0.41$, respectively. Asymmetric steady-state solution branches, that bifurcate from the symmetric steady-state solutions at the zero eigenvalue crossings, are also shown. Additional periodic solution branches, arising from Hopf bifurcations off of these asymmetric steady-states, also occur.

For a fixed $L/l_0 = 0.4$, and with $q = 5$, $z = 3.5$, $\tau_v = 200$, and $\epsilon = 0.3$, in the right panel of Fig. 12 we plot the bifurcation diagram of u with respect to l_1/l_0 , showing the primary solution branches and some secondary bifurcations. This plot corresponds to taking a vertical slice in the phase diagram given in the left panel of Fig. 12. There are several key features in this plot. Firstly, as l_1/l_0 is increased from zero, the first bifurcation is to synchronous temporal oscillations.

Our computations show that, except in very narrow ranges of l_1/l_0 , the global branch of synchronous oscillations between the two membranes is stable. Secondly, we observe that the asynchronous branch of oscillations that bifurcates from the symmetric steady-state at $l_1/l_0 \approx 0.41$ is unstable. Thirdly, the asymmetric steady-state solution branch bifurcates from the symmetric steady-state branch at two values of l_1/l_0 . These asymmetric steady-states are mostly unstable, but there is a range of l_1/l_0 where they are stable. Mostly unstable periodic solution branches, emerge from, and terminate on, the asymmetric steady-state branch. Overall, the bifurcation diagram is rather intricate, and it is beyond the scope of this paper to classify and study all of these secondary bifurcations.

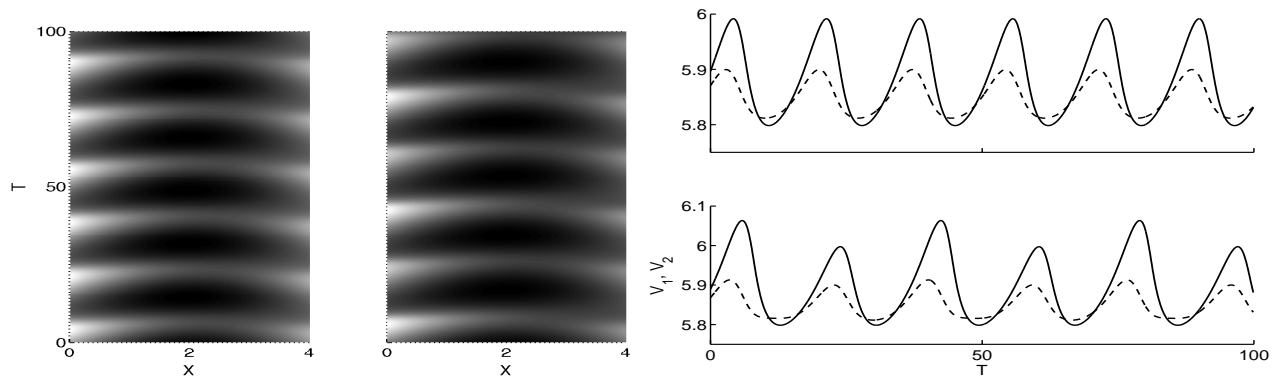


Figure 13. Left panel: Contour plot of $V(x, t)$ computed numerically from the PDE-ODE system (3.1) for $l_1/l_0 \approx 0.406$ ($k_v = 1.22$) (left) and for $l_1/l_0 \approx 0.41$ ($k_v = 1.23$) (right). The initial condition is $V(x, 0) = 0.5$, $u_1 = 1$, $u_2 = 5$, $v_1 = v_2 = 0.5$, at $t = 0$. The system exhibits synchronized oscillations with unequal amplitude for $l_1/l_0 \approx 0.406$, and synchronized period-doubling oscillations for $l_1/l_0 \approx 0.41$. The other parameters are the same as in Fig. 12. Right panel: The inhibitor concentrations $v_1(t)$ and $v_2(t)$ in the two membranes for $l_1/l_0 \approx 0.406$ (top) and for $l_1/l_0 \approx 0.41$ (bottom).

From the right panel in Fig. 12, we observe that although the synchronous periodic solution branch is stable in a large range of l_1/l_0 , there is a narrow region $0.413 < l_1/l_0 < 0.430$ predicted by XPPAUT [7] where the symmetric steady-state and the synchronous periodic solution branch are both unstable. As a result, in this narrow region we anticipate that (3.1) will exhibit rather complex dynamics. Due to the small numerical error associated with using XPPAUT on the spatially discretized version of (3.1), in our numerical simulations of the PDE-ODE system (3.1) shown in Fig. 13 we have observed qualitatively interesting dynamics in a slightly shifted interval of l_1/l_0 . The results in Fig. 13 are for $l_1/l_0 = 0.406$ and for $l_1/l_0 = 0.41$. From Fig. 13, we conclude that as l_1/l_0 is increased through the narrow zone where the synchronous branch is unstable, the two membranes first exhibit synchronized oscillations with a significant distinction in their oscillating amplitudes. This is followed by period-doubling behavior. As l_1/l_0 increases further, the period-doubling behavior disappears and the two membranes return to synchronous oscillations with unequal amplitudes.

In comparison with the phase diagram of Fig. 6 for the singular limit case $\epsilon \rightarrow 0$, Fig. 12 shows that the parameter range where asynchronous instabilities occur lies distinctly within the corresponding synchronous range. The global bifurcation diagram in the right panel of Fig. 12 shows that it is only the synchronous branch of oscillations that is typically linearly stable. Secondary instabilities, only partly explored, emerging from the branch of asymmetric steady-state solutions and the asynchronous oscillatory solution branch suggests the possibility of more exotic period-doubling and mixed-mode behavior.

4 Two Diffusive Species in the Bulk

In §3 we assumed that only the inhibitor can detach from the membrane and diffuse in the bulk. In this section, we consider the full model (1.1) where both the activator and inhibitor undergo bulk diffusion. To partially restrict the wide parameter space for (1.1), we will study (1.1) for the fixed parameter values, which are taken largely from [9], given by

$$(4.1 a) \quad D_v = 0.5, \quad D_u = 1.5, \quad \sigma_v = 0.008, \quad \sigma_u = 0.01, \quad z = 3.5, \quad q = 5,$$

and we will impose equal leakages that $k \equiv k_u = k_v$. We then introduce the diffusion lengths l_0 and l_u , the ratio of diffusion lengths α_u , and the two time-constants τ_v and τ_u , by

$$(4.1 b) \quad l_0 \equiv \sqrt{\frac{D_v}{\sigma_v}} \approx 7.9057, \quad l_u \equiv \sqrt{\frac{D_u}{\sigma_u}} \approx 12.247, \quad \alpha_u \equiv \frac{l_0}{l_u} \approx 0.6455, \quad \tau_v \equiv \frac{1}{\sigma_v} = 125, \quad \tau_u \equiv \frac{1}{\sigma_u} = 100.$$

We let the domain length L and the common leakage k to be our bifurcation parameters, and define $l_1 = k/\epsilon$ with $\epsilon = 0.15$. Below we determine phase diagrams in the parameter space l_1/l_0 versus L/l_0 where membrane-bulk oscillations occur.

To determine the stability of the unique symmetric steady-state solution, we first nondimensionalize (2.17), in a similar way as was done in (3.7) for the one-bulk species model. We obtain that the number N of eigenvalues λ of the linearization of (1.1) in $\text{Re}(\lambda) > 0$ is

$$(4.2) \quad N = P + \frac{1}{\pi} [\arg \mathcal{F}_{\pm}^0]_{\Gamma_+}, \quad \text{where} \quad P = \begin{cases} 2 & \text{if } b = \text{tr} J_e > 0 \\ 0 & \text{if } b = \text{tr} J_e < 0 \end{cases}, \quad b \equiv 1 - \epsilon - 3q(u_e - 2)^2,$$

where u_e is the unique root of the cubic (2.3 a), and where $\mathcal{F}_{\pm}^0(\lambda)$ is defined by

$$(4.3 a) \quad \mathcal{F}_{\pm}^0(\lambda) \equiv \frac{l_0}{l_1 q_{\pm}} - \frac{\epsilon \sqrt{1 + \tau_v \lambda} (b + \epsilon - \lambda)}{\det(J_e - \lambda I)} + \frac{\epsilon \alpha_u \sqrt{1 + \tau_u \lambda} (\epsilon + \lambda)}{\det(J_e - \lambda I)} \left(\frac{p_{\pm}}{q_{\pm}} \right) + \left(\frac{\epsilon^2 \alpha_u l_1}{l_0} \right) p_{\pm} \frac{\sqrt{1 + \tau_v \lambda} \sqrt{1 + \tau_u \lambda}}{\det(J_e - \lambda I)}.$$

Here $\det(J_e - \lambda I) = \lambda^2 - b\lambda + \epsilon(z - \epsilon - b)$, q_{\pm} are given in (3.8), and p_{\pm} are defined by

$$(4.3 b) \quad p_+ = \tanh \left(\alpha_u \sqrt{1 + \tau_u \lambda} \frac{L}{2l_0} \right), \quad p_- = \coth \left(\alpha_u \sqrt{1 + \tau_u \lambda} \frac{L}{2l_0} \right).$$

We observe that the first two-terms in (4.3 a) are the same as in (3.7), with the last two terms arising from the additional coupling with the activator. As in §3.1, it is possible to study (4.3) in the limit $\epsilon \rightarrow 0$ to determine N analytically for both the synchronous and asynchronous modes, and to asymptotically calculate the Hopf bifurcation frequencies near onset. However, in this section, we will consider the finite ϵ problem with $\epsilon = 0.15$ and use Maple [19] to numerically compute both the roots of (4.3) and the winding number in (4.2), which gives N .

In this way, in the left panel of Fig. 14 we show a phase diagram in the l_1/l_0 versus L/l_0 parameter space, where $l_1 = k/\epsilon$ and $\epsilon = 0.15$, with $k \equiv k_v = k_u$. The Hopf bifurcation boundaries for the synchronous and asynchronous modes are the solid and dashed curves, respectively. Inside the region bounded by the disjoint solid curves, the synchronous mode is unstable with two unstable eigenvalues. Inside the open loop bounded by the dashed curve, the asynchronous mode is unstable with $N = 2$. In contrast to the phase diagrams for the one-bulk species case, no zero-eigenvalue crossings were detected for the parameter set (4.1). This aspect is discussed further at the end of this section.

By using XPPAUT [7], in the right panel of Fig. 14 we plot the global bifurcation diagram of u with respect to l_1/l_0 for a fixed vertical slice with $L = 4$ through the phase diagram in the left panel of Fig. 14, so that $L/l_0 \approx 0.505$. This plot shows that the synchronous mode first loses stability to a stable periodic solution at $l_1/l_0 \approx 0.36$, and that there is a subsequent Hopf bifurcation to the asynchronous mode at $l_1/l_0 \approx 0.39$. The key feature in this plot is that the synchronous branch of periodic solutions is almost entirely stable, while the asynchronous branch is unstable. No asymmetric steady-state

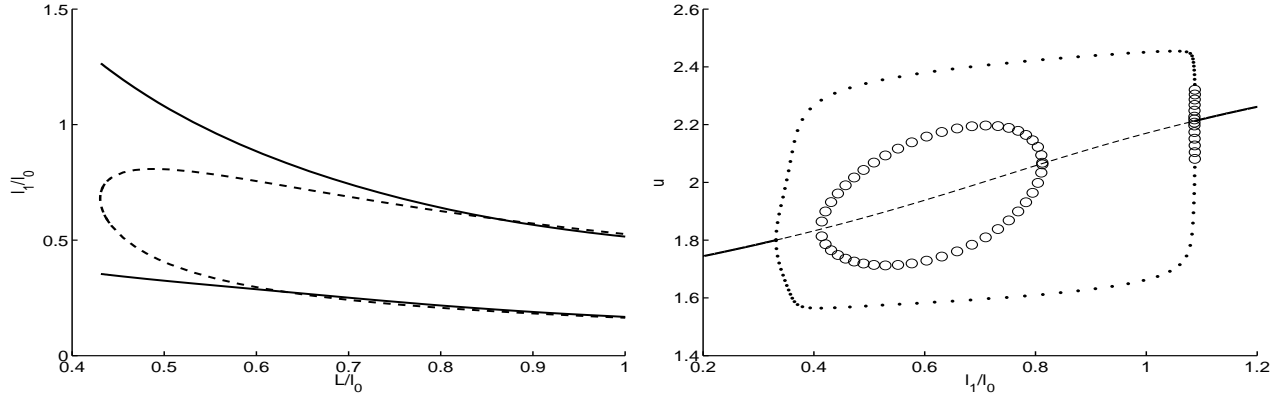


Figure 14. Left panel: The Hopf bifurcation boundaries for the synchronous mode (solid curves) and asynchronous mode (dashed curves) for the two-bulk species model (1.1), as computed from (4.3) with Maple [19] when $\epsilon = 0.15$ and for the parameters of (4.1). Inside the region bounded by the solid curves, the synchronous mode is unstable, while inside the region bounded by the dashed loop the asynchronous mode is unstable. Right panel: Global bifurcation diagram of u with respect to l_1/l_0 for fixed $L = 4$ so that $L/l_0 \approx 0.505$. The solid/dashed lines are stable/unstable symmetric steady-states. The outer loop, which is almost entirely stable, corresponds to the branch of synchronous oscillations. The inner loop is the unstable branch of asynchronous oscillations.

solutions bifurcating from the symmetric steady-state branch were detected. As a partial confirmation of these theoretical predictions, in Fig. 1 of §1 we showed a contour plot of $V(x, t)$ computed from the PDE-ODE system (1.1) for the parameters of (4.1) and with $\epsilon = 0.15$, $L = 4$, $k = 0.7$, so that $L/l_0 \approx 0.505$ and $l_1/l_0 \approx 0.59$. With a random initial condition, this plot shows the eventual synchronization of the oscillations in the two membranes. This simulation of §1 confirms the prediction of the right panel of Fig. 14 that only the synchronous mode is stable for this parameter choice.

We remark that richer spatio-temporal dynamics can occur if we choose a vertical slice through the phase diagram in the left panel of Fig. 14 for the larger value $L = 5.5$, so that $L/l_0 \approx 0.70$. In the right panel of Fig. 15 we plot the global bifurcation diagram of u versus l_1/l_0 for this vertical slice. In contrast to the case where $L = 4$ in the right panel of Fig. 14, we observe from Fig. 15 that, as we increase the value of l_1/l_0 from 0.2, the asynchronous mode loses its stability before the synchronous mode. However, as l_1/l_0 is decreased from 0.8, the synchronous mode loses its stability at $l_1/l_0 \approx 0.76$ before the asynchronous mode at $l_1/l_0 \approx 0.70$. We again find that the synchronous mode is stable for a wide range of l_1/l_0 . However, in the rather narrow parameter range $0.290 < l_1/l_0 < 0.305$ both the synchronous and asynchronous modes are unstable. To examine the behavior of the full PDE-ODE system (1.1) in this range of l_1/l_0 , in the left panel of Fig. 15 we plot the numerically computed time evolution of $v_2(t) = V(L, t)$ for (1.1) when $l_1/l_0 = 0.30$. The initial conditions used in the simulation are the same as given in the caption of Fig 1. The resulting time-series for $v_2(t)$ shows the presence of two distinct periods, which is indicative of a torus bifurcation. The analysis of such co-dimension-2 bifurcations is beyond the scope of this paper. For a related coupled membrane-bulk model, with Sel'kov dynamics on the membrane, a normal form analysis of such torus bifurcations was given in [10].

Finally, we confirm theoretically that there are no zero-eigenvalue crossings, corresponding to the bifurcation of asymmetric steady-state solutions from the symmetric steady-state branch. Proceeding similarly as in (3.26)–(3.27 b) of §3.1, we obtain in place of (3.27 b) that, for any asymmetric steady-state solution of (1.1), $\mathbf{u} = (u_1, u_2)^T$ now satisfies

$$(4.4) \quad -q \begin{pmatrix} (u_1 - 2)^3 \\ (u_2 - 2)^3 \end{pmatrix} + 4 \begin{pmatrix} 1 \\ 1 \end{pmatrix} + \mathbf{u} - z\mathcal{A}^{-1}\mathbf{u} = \frac{k}{l_u}\mathcal{B}\mathbf{u}, \quad \mathcal{B} \equiv \begin{pmatrix} \coth\left(\frac{L}{l_u}\right) & -\operatorname{csch}\left(\frac{L}{l_u}\right) \\ -\operatorname{csch}\left(\frac{L}{l_u}\right) & \coth\left(\frac{L}{l_u}\right) \end{pmatrix}.$$

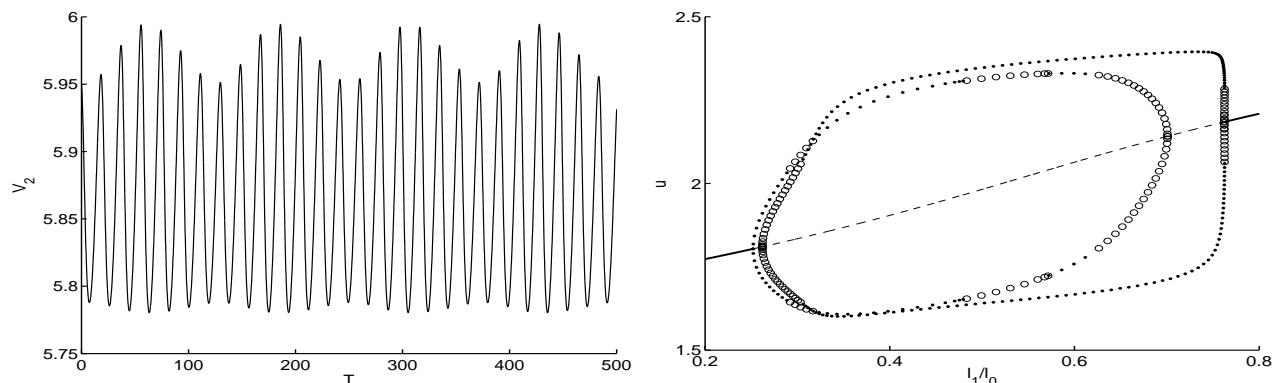


Figure 15. Left panel: Plot of $v_2(t) = V(L, t)$ versus t computed from full PDE-ODE system (1.1) for the parameter values of (4.1) and with $\epsilon = 0.15$, $L = 5.5$, $k = 0.35$, so that $L/l_0 \approx 0.7$ and $l_1/l_0 \approx 0.30$. The resulting time series has two distinct periods, which indicates a possible torus bifurcation where the in-phase and anti-phase periodic solutions change from stable (unstable) to unstable (stable). Right panel: Global bifurcation diagram of u with respect to l_1/l_0 for fixed $L = 5.5$, so that $L/l_0 \approx 0.7$. The labeling of the branches and their stability is the same as in the right panel of Fig. 14. The closed, primarily outer, loop is the synchronous branch, while the other closed loop is the asynchronous branch, which is mostly unstable. The synchronous branch is again mostly stable. In the window $0.290 < l_1/l_0 < 0.305$ both the synchronous and asynchronous branches of periodic solutions are unstable. No secondary bifurcations are shown.

where \mathcal{A} is defined in (3.27 a). Since \mathcal{B} is symmetric with a constant row sum, the eigenvectors $\mathbf{q}_1 = (1, 1)^T$ and $\mathbf{q}_2 = (1, -1)^T$ are common to both \mathcal{A} and \mathcal{B} . The two eigenvalues of \mathcal{B} are $\xi_1 = \tanh(L/(2l_u))$ and $\xi_2 = \coth(L/(2l_u))$.

The symmetric steady-state solution is recovered by seeking a solution to (4.4) of the form $\mathbf{u} = u_e \mathbf{q}_1$. By using the explicit expressions for the eigenvalues ξ_1 and μ_1 of \mathcal{B} and \mathcal{A} , respectively, where μ_1 is given in (3.28), we readily derive that u_e satisfies the cubic (2.3 a). To determine whether there are any bifurcation points from this branch we write $\mathbf{u} = u_e(1, 1)^T + \delta\phi$ for $\delta \ll 1$, and linearize (4.4). We conclude that bifurcation points occur whenever

$$(4.5) \quad -3q(u_e - 2)^2\phi + \phi - z\mathcal{A}^{-1}\phi - \frac{k}{l_u}\mathcal{B}\phi = 0,$$

has a nontrivial solution ϕ . For the in-phase mode $\phi = \mathbf{q}_1$, we use the explicit expressions for ξ_1 and μ_1 to derive from (4.5) that any such bifurcation point must satisfy $\beta + a_u - 1 = -3q(u_e - 2)^2$, where β and a_u are defined in (2.3 b). By an identical proof as in §3.1, this condition is inconsistent with any root u_e to the cubic (2.3 a). Thus, no zero-eigenvalue crossing of the in-phase mode from the symmetric steady-state branch can occur.

For the anti-phase mode $\phi = \mathbf{q}_2$, we use the explicit expressions for the eigenvalues ξ_2 and μ_2 in (4.5) to obtain that there is a bifurcation point to an asymmetric steady-state whenever

$$-3q(u_e - 2)^2 + 1 - \frac{k}{l_u}\coth\left(\frac{L}{2l_u}\right) = \frac{z}{1 + \frac{l_1}{l_0}\coth\left(\frac{L}{2l_0}\right)},$$

has a solution, where u_e is a root of the cubic (2.3 a). For the parameter set (4.1), we verified numerically that no such solution exists for any point in the phase diagram in the left panel of Fig. 14. However, we remark that for other parameter sets, notably when ϵ is decreased from $\epsilon = 0.15$, such bifurcation points should be possible.

5 Discussion

By using a combination of asymptotic analysis, spectral theory, and the numerical bifurcation software XPPAUT [7], we have examined the existence and stability of oscillatory dynamics for the membrane-bulk system (1.1). We refer to such

oscillations as triggered oscillations, since in the absence of membrane-bulk coupling we have assumed that the membrane dynamics have a stable fixed point. Our asymptotic analysis has been based on exploiting the asymptotic limit of a slow-fast structure of the membrane-bulk coupling, and in contrast to the previous studies of [27] and [25] on related PDE-ODE models with applications to neuroscience, is not based on the assumption of a weak coupling between the membrane and the bulk. Qualitatively, our phase diagrams in Figs. 6, 12, and 14 based on the linear stability properties of the steady-state, have shown that oscillatory dynamics in the two membranes, triggered by bulk diffusion, only occurs for some intermediate range of the membrane-bulk leakage parameter. In the non-singularly perturbed limit where $\epsilon = \mathcal{O}(1)$, we have shown that the parameter range where synchronous oscillations can occur between the two membranes is significantly larger than that for asynchronous oscillations. Moreover, our numerical computations of global bifurcation diagrams have revealed that there are large parameter regions where it is only the bifurcating branch of synchronous oscillations that is linearly stable. Overall, our linear stability analysis, augmented by the computation of global branches of periodic solutions, indicates that stable large-amplitude synchronized oscillations is a robust feature in the dynamics of the coupled membrane-bulk model (1.1). Similar qualitative results, showing a wide parameter range where stable synchronized oscillations occur, have been found in [12] and [11] for other membrane kinetics.

As possible extensions of this study, it would be interesting to use Floquet theory to investigate oscillatory dynamics for a chain of dynamically active membranes localized on lattice sites that are coupled by bulk diffusion. Such models are related to the study of cascades in cellular signal transduction (cf. [15]), and the study of the effect of catalysts on dynamically active surfaces (cf. [24], [28]). A particular problem of this type is considered in [11] for the case of Sel'kov membrane kinetics. It would also be worthwhile to study large-scale oscillations by representing the bulk diffusion field in terms of a time-dependent Green's function with memory. Coupling to the membrane dynamics would lead to a continuously distributed delay equation for the dynamically active membrane components. Moreover, it would be interesting to develop detailed models of the leakage term so as construct switches or bursters through which the oscillatory dynamics can be turned on or off. Two such possibilities include allowing the leakage parameter to depend on time through an additional slow variable, or to allow it to switch stochastically via a Markov jump process between an on and off state. The first possibility is related to slow passage through Hopf bifurcations (cf. [3], [4], [18]), while the second possibility is related to analyzing stochastic hybrid systems with stochastic switching of the boundary conditions (cf. [5], [14]).

From a numerical viewpoint, it would also be interesting to use numerical bifurcation software to give a detailed investigation of secondary instabilities arising from bifurcations of asymmetric steady-state solutions or either the synchronous or asynchronous periodic solution branch. Our preliminary results show that such secondary bifurcations can lead to more exotic dynamics such as quasi-periodic solutions or period-doubling behavior. In particular, it would be interesting to explore whether there can be any period-doubling route to chaotic dynamics such as was observed computationally in [22] for a related model consisting of two diffusing bulk species that are subject to nonlinear fluxes at fixed lattice sites.

Finally, we remark that models for the coupling of dynamically active, spatially segregated, reaction "cells" through a three-dimensional bulk diffusion field have been introduced and studied in [20] and [21], with applications to modeling quorum-sensing behavior in all of \mathbb{R}^3 . In a 2-D bounded domain, in [13] the strong localized perturbation theory of [30], which is valid in the limit of small cell radius, was used both for constructing steady-state solutions and for analyzing their linear stability properties. In this way, in [13] parameter regimes where synchronous oscillations between the cells can occur as a result of the bulk-cell coupling have been identified for various choices of the intracellular kinetics.

Acknowledgements

Michael J. Ward gratefully acknowledges the grant support of NSERC.

References

- [1] J. C. Alexander, *Spontaneous Oscillations in Two 2-Component Cells Coupled by Diffusion*, J. Math. Biol., **23**(2), (1986), pp. 205–219.
- [2] P. Ashwin, S. Coombes, R. Nicks, *Mathematical Frameworks for Oscillatory Network Dynamics in Neuroscience*, submitted, arXiv:1506.05828, (2015) (99 pages).
- [3] S. M. Baer, T. Erneux, J. Rinzel, *The Slow Passage Through a Hopf bifurcation: Delay, Memory Effects, and Resonance*, SIAM J. Appl. Math., **49**(1), (1989), pp. 5571.
- [4] R. Bertram, M. J. Butte, T. Kiemel, A. Sherman, *Topological and Phenomenological Classification of Bursting Oscillations*, Bull. Math. Bio. **57**(3), (1995), pp. 413–439.
- [5] P. C. Bressloff, S. D. Lawley, *Escape From Subcellular Domains with Randomly Switching Boundaries*, to appear, SIAM Mult. Model. Sim., (2015).
- [6] W. Y. Chiang, Y. X. Li, P. Y. Lai, *Simple Models for Quorum Sensing: Nonlinear Dynamical Analysis*, Phys. Rev. E., **84**, (2011), 041921.
- [7] G. B. Ermentrout, *Simulating, Analyzing, and Animating Dynamical Systems: A Guide to XPPAUT for Researchers and Students*, SIAM 2002, Philadelphia, USA.
- [8] A. Goldbeter, *Biochemical Oscillations and Cellular Rhythms: The Molecular Bases of Periodic and Chaotic Behaviour*, Cambridge U. Press, Cambridge, U.K. (1990), 632 pp.
- [9] A. Gomez-Marin, J. Garcia-Ojalvo, J. M. Sancho, *Self-Sustained Spatiotemporal Oscillations Induced by Membrane-Bulk Coupling*, Phys. Rev. Lett., **98**(16), (2007), 168303.
- [10] J. Gou, Y. X. Li, W. Nagata, *Interactions of In-Phase and Anti-Phase Synchronies in Two Cells Coupled by a Spatially Diffusing Chemical: Double-Hopf Bifurcations*, accepted, IMA J. Appl. Math., (2015), (20 pages).
- [11] J. Gou, W. Y. Chiang, P. Y. Lai, M. J. Ward, Y. X. Li, *A Theory of Synchrony by Coupling Through a Diffusive Medium*, to be submitted, Phys. Rev. E. (2016), (22 pages).
- [12] J. Gou, Y. X. Li, W. Nagata, M. J. Ward, *Synchronized Oscillatory Dynamics for a 1-D Model of Membrane Kinetics Coupled by Linear Bulk Diffusion*, to appear, SIAM J. Appl. Dyn. Sys., (2015), (35 pages).
- [13] J. Gou, M. J. Ward, *An Asymptotic Analysis of a 2-D Model of Dynamically Active Compartments Coupled by Bulk Diffusion*, submitted, J. Nonl. Science, (2015), (37 pages).
- [14] S. D. Lawley, J. C. Mattingly, M. C. Reed, *Stochastic Switching in Infinite Dimensions with Application to Random Parabolic PDE's*, SIAM J. Math. Anal., **47**(4), (2015), pp. 3035-3063.
- [15] B. N. Kholodenko, *Cell-Signalling Dynamics in Time and Space*, Nat. Rev. Mol. Cell Biol., **7**, (2006), pp. 165–176.
- [16] D. Kulginov, V. P. Zhdanov, B. Kasemo, *Oscillatory Surface Reaction Kinetics due to Coupling of Bistability and Diffusion Limitations*, J. Chem. Phys., **106**, (1997), 3117.
- [17] H. Levine, W. J. Rappel, *Membrane Bound Turing Patterns*, Phys. Rev. E., **72**, (2005), 061912.
- [18] P. Mandel, T. Erneux, *The Slow Passage Through a Steady Bifurcation: Delay and Memory Effects*, J. Stat. Physics, **48**(5-6), (1987), pp. 1059–1070.
- [19] Maple 14, *Maplesoft, a division of Waterloo Maple Inc.*, Waterloo, Ontario.
- [20] J. Müller, H. Uecker, *Approximating the Dynamics of Communicating Cells in a Diffusive Medium by ODEs - Homogenization with Localization*, J. Math. Biol., **67**(5), (2013), pp. 1023–1065.
- [21] J. Müller, C. Kuttler, B. A. Hense, M. Rothballer, A. Hartmann, *Cell-Cell Communication by Quorum Sensing and Dimension-Reduction*, J. Math. Biol., **53**(4), (2006), pp. 672–702.
- [22] F. Naqib, T. Quail, L. Musa, H. Vulpe, J. Nadeau, J. Lei, L. Glass, *Tunable Oscillations and Chaotic Dynamics in Systems with Localized Synthesis*, Phys. Rev. E., **85**, (2012), 046210.
- [23] H. Nakao, *Phase Reduction Approach to Synchronization of Nonlinear Oscillators*, Contemporary Physics, online first, Oct. 2015.
- [24] A. P. Peirce, H. Rabitz, *Effect of Defect Structures on Chemically Active Surfaces: A Continuum Approach*, Phys. Rev. B., **38**(3), (1998), pp. 1734–1753.
- [25] M. Remme, M. Lengyel, B. Gutkin, *The Role of Ongoing Dendritic Oscillations in Single-Neuron Dynamics*, PLoS Computational Biology, **5**(9), (2009), p. e1000493.
- [26] H. Riecke, L. Kramer, *Surface-Induced Chemical Oscillations and their Influence on Space- and Time- Periodic Patterns*, J. Chem. Physics., **83**, (1985), 3941.
- [27] M. A. Schwemmer, T. J. Lewis, *The Robustness of Phase-Locking in Neurons with Dendro-Dendritic Electrical Coupling*, J. Math. Biol., **68**(1), (2014), pp. 303–340.
- [28] S. Y. Shvartsman, E. Schütz, R. Imbihl, I. G. Kevrekidis, *Dynamics of Microcomposite Catalytic Surfaces: The Effect of Active Boundaries*, Phys. Rev. Lett., **83**, (1999), 2857.
- [29] S. Smale, *A Mathematical Model of Two Cells via Turing's Equation*, J.D. Cowan (ed.) Some Mathematical Questions in Biology. V. American Mathematical Society Lectures on Mathematics in the Life Sciences, **6**, (1974), pp. 15–26.
- [30] M. J. Ward, *Asymptotics for Strong Localized Perturbations: Theory and Applications*, online lecture notes for *Fourth Winter School on Applied Mathematics*, CityU of Hong Kong, (2010).